# Sensitivity of simulated circulation dynamics to the choice of surface wind forcing in the Japan/East Sea

Patrick J. Hogan*, Harley E. Hurlburt

*Naval Research Laboratory, Stennis Space Center, MS 39529, USA*

## Abstract

The circulation sensitivity to the choice of wind-forcing product is investigated with the NRL Layered Ocean Model (NLOM) configured for the Japan/East Sea. Monthly climatologies from seven different wind-stress data sets (and wind-stress curl) are formed from observed and model-derived atmospheric data sets. The resulting maps of wind-stress curl reveal significantly different spatial patterns and magnitudes, even two with largely opposite large-scale patterns of wind-stress curl. These wind sets were used in forcing three sets of simulations, $1/8°$ linear and $1/8°$ and $1/32°$ nonlinear. In addition, seasonally varying straits forcing (inflow through Tsushima balanced by outflow through Tsugaru and Soya) was included in all the simulations, and simulations with straits forcing only were performed. The 1.5-layer linear reduced-gravity simulations include only the lowest order dynamics, mainly Munk $\beta^{1/3}$ western boundary layers (due to both wind and straits forcing) and a Sverdrup interior. The nonlinear simulations add bottom topography, multiple internal modes, diapycnal mixing, and ventilation of layer interfaces. At $1/8°$ resolution, only weak barotropic/ baroclinic instabilities occur, but at $1/32°$ resolution these are much stronger, allowing vigorous transfer of energy from the upper ocean to the abyssal layer via baroclinic instability. This drives much stronger mean abyssal currents that more strongly steer upper-ocean current pathways than at $1/8°$, i.e. there is much stronger upper ocean–topographical coupling. The linear model simulates most of the basic features, e.g., the subpolar gyre with all but the straits forcing only, the East Korean Warm Current (EKWC) and its connection to the subpolar front with all but one wind-forcing set, but the remaining wind set gives a continuous Nearshore Branch (NB) of the Tsushima Warm Current along the coast of Honshu. In all of the linear simulations with an EKWC, the separation latitude from the coast of Korea is determined by the latitude ($\sim41°$N) of the Tsugaru Strait outflow (too far north) except for one, which is also too far north. All of the nonlinear simulations include the NB, which is mainly due to isopycnal outcropping. This creates another inflow to outflow pathway, diverting some of the flow from the EKWC and allowing the wind-stress curl to compete better with straits forcing in determining the EKWC separation latitude. Using the $1/8°$ nonlinear model, three of the wind-forcing sets yield a realistic separation latitude for the EKWC ($\sim37–38°$N) and two more are marginally successful. The two remaining and the simulation with straits forcing only yield EKWC overshoot to $\sim40°$N. At $1/32°$ resolution, one of the simulations (one with forcing that gave marginally realistic separation at $1/8°$) has a realistic EKWC separation latitude. The three wind products that yielded realistic EKWC separation at $1/8°$ continue to give

---

*Corresponding author.

*E-mail address:* pat.hogan@nrlssc.navy.mil (P.J. Hogan).

realistic separation at $1/32°$ via the wind-stress curl, but the remainder give realistic separation via upper ocean–topographical coupling. At $1/32°$ resolution all but one of the simulations showed a strong Yamato Rise impact on the pathway of the subpolar front due to steering by abyssal currents. At $1/8°$ resolution only two of the eight showed any such impact, one due to abyssal currents driven by vertical mixing in the subpolar gyre. In all the other $1/8°$ simulations the mean abyssal currents were weak, but in one case weak abyssal currents were aided by a region of strong negative wind-stress curl not seen in the other wind products. In addition, regions of the ventilation of intermediate and deep water in response to each wind set are identified. A series of six $1/32°$ simulations forced interannually with 6-hourly winds 1979–93 are used to separate the model variability due to wind forcing (deterministic) and flow instabilities (nondeterministic). This analysis indicates that flow instabilities are the dominant source of SSH variability over a large majority of the basin, especially near 37–38°N, where the EKWC separates from the coast, and along the pathway of the subpolar front following the north rim of the Yamato Rise towards the Tsugaru Strait. Wind forcing dominates the SSH variability in the coastal wave guide and over the deep basins and troughs.
Published by Elsevier Ltd.

## 1. Introduction

The circulation in the Japan/East Sea (JES, hereafter) can be significantly influenced by many physical factors, including inflow through the Tsushima/Korea Strait (with accompanying out-flow through Tsugaru and Soya Straits), surface wind forcing, surface buoyancy forcing (heating and cooling, salt- and fresh-water fluxes), and the bottom topogaphy. There are also dynamical factors that affect the circulation, such as iso-pycnal outcropping and barotropic and baroclinic flow instabilities. These factors impact the surface and deep circulation on different space and time scales, ranging from sub-mesoscale to interannual. All are believed to have a significant impact on the location and strength of the large-scale circulation features. In recent years much greater knowledge and understanding of the mean current structures in the JES have evolved, but so has the recognition that there is a rich mesoscale eddy field and that even the large-scale current systems exhibit significant variability over a wide range of frequencies. However, several schematics of the general JES circulation provide a guide for evaluating JES modeling efforts. The schematic shown in Fig. 1 depicts the mean surface circula-tion features, including the East Korean Warm Current (EKWC) (a branch of the Tsushima Warm Current (TWC)), the Liman and North Korea Cold Currents (LCC and NKCC, respec-tively), the subpolar front, and the Nearshore Branch (NB) of the TWC. Other schematics of the

JES show slight variations or more detail, as shown by Naganuma (1977) and Yarachin (1980), but the large-scale features are similar.
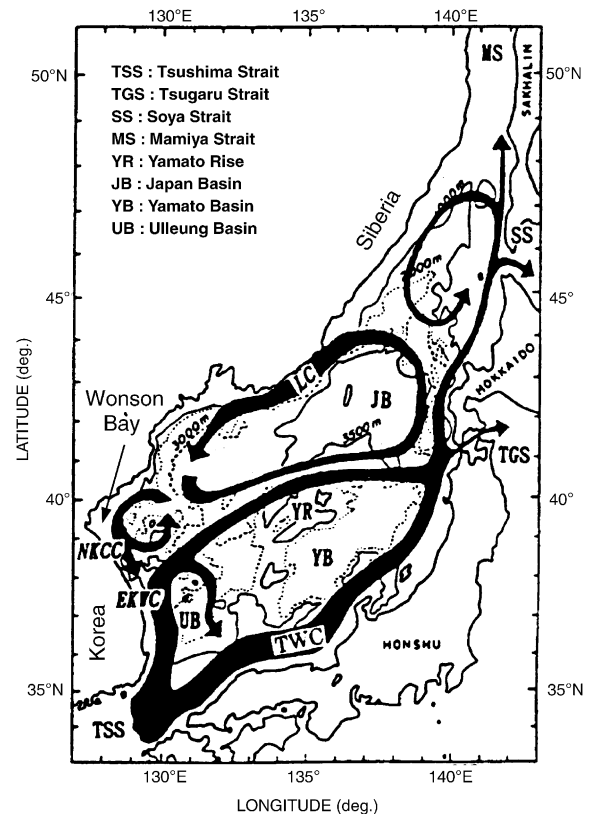


Fig. 1. Schematic map for sea-surface currents in the JES. Abbreviations explained within figure. From Morimoto and Yanagi (2001), after Senjyu (1999).

To lowest order, ocean dynamics are largely governed by the wind-stress curl through the Sverdrup relation. Ocean circulation models, therefore, require the surface wind-stress or its curl as a specified boundary condition, and climatological fields are commonly used. Several modeling studies in the JES have been undertaken in the last two decades, including pioneering studies by Yoon (1982) and Kawabe (1982), and more recently studies by Sekine (1991), Seung and Kim (1993), Holloway et al. (1995), Kim and Yoon (1999), and Hogan and Hurlburt (2000). These modeling studies yield a wide range of numerical solutions that can be compared to observations or schematic diagrams such as Fig. 1 to assess their performance, but the variety of ocean model designs, configurations, and forcing functions can make it difficult to distill the source of the differences and to determine which have the greatest impact.

In this paper, all of the simulations include the throughflow forcing via the straits. Given this, we show that the choice among seven different monthly wind-forcing products can have a profound impact on numerical ocean model simulations of all the current systems shown in Fig. 1 plus many other features of the circulation, including the abyssal circulation. For example, some give realistic separation of the EKWC from the east coast of Korea, while others do not. In addition to wind-stress curl, Hogan and Hurlburt (2000) (hereafter HH2000) discovered another mechanism for realistic separation of the EKWC, upper ocean–topographical coupling via baroclinic instability. Either mechanism by itself can be sufficient to give realistic EKWC separation and to impact many other features of the circulation, but HH2000 needed $1/32°$ resolution for each model variable to obtain EKWC separation via the upper ocean–topographical coupling mechanism alone and for this mechanism to have a major impact on the overall circulation.

In this paper, the role of wind forcing in the absence and presence of upper ocean–topographical coupling is investigated by performing simulations with the Naval Research Laboratory (NRL) Layered Ocean Model (NLOM) at $1/8°$ and $1/32°$ resolutions, respectively. Specifically, at $1/8°$ resolution we have performed two sets of eight simulations (seven simulations for each of the monthly wind-stress climatologies and one with no wind forcing). The first set is linear, 1.5-layer reduced gravity, and includes only the lowest order dynamics, basically a Sverdrup (1947) interior with Munk (1950) $\beta^{1/3}$ western boundary layers due to both wind and throughflow forcing. The second set is moderately nonlinear and adds bottom topography, multiple internal modes, diapycnal mixing and ventilation of the Lagrangian model layers (buoyancy forcing is neglected). These additions allow the possibility of barotropic/baroclinic flow instabilities, the formation of inertial jets and boundary layers, and isopycnal outcropping. A similar set of simulations was performed at $1/32°$, except that the simulations forced by the Comprehensive Ocean–Atmosphere Data Set (COADS) and throughflow only are omitted due to the similarity of the simulations with the HR-forced simulation at $1/8°$ resolution. The impact of increased horizontal grid resolution is discussed in Section 6.

## 2. The NRL Layered Ocean Model

NLOM is a semi-implicit primitive-equation ocean model that casts the layered model equations in transport form. The model retains the free surface and can include realistic bottom topography as long as it is restricted to the lowest layer. The original model design is described in Hurlburt and Thompson (1980), and significant enhancements are described in Wallcraft (1991), Wallcraft and Moore (1997), and Moore and Wallcraft (1998), including an implementation in spherical coordinates.

All of the nonlinear simulations used in this study have four Lagrangian layers in the vertical with interfaces initially situated at 60, 130, and 250 m with density differences ($\sigma_\Theta$) across each interface of 0.80, 0.32, and 0.42, respectively. The comparisons using different atmospheric forcings are done at both $1/8°$ and $1/32°$ horizontal resolutions between like variables on a C-grid. The role of the $1/8°$ simulations is to limit the impact of flow instabilities while maintaining sufficient nonlinearity to assess its impact on the response of

current systems to atmospheric forcing. The $1/32°$ simulations include the impact of the different wind forcing as well as higher-order dynamics (such as upper ocean–topographical coupling), as described in HH2000. An additional suite of simulations with $1/32°$ resolution is used to assess the impact of flow instabilities, and wind/straits forcing on the variability is described in Section 7. Aside from the grid resolution ($1/8°$ vs. $1/32°$), the only other physical (vs. dynamical) difference is the horizontal eddy viscosity (50 vs. $5\,m^2/s$). Although thermodynamic versions of the model exist, all the simulations used here are purely hydrodynamic, i.e. they contain no horizontally varying density gradients within a layer. Holloway et al. (1995) found buoyancy forcing to be less significant relative to wind forcing, at least for the large-scale surface circulation. That claim is not made here, since all of the simulations in this study exclude buoyancy forcing; rather the focus of this paper is the response to the wind forcing.

For all simulations, the throughflow is provided via open boundary conditions at the Tsushima/ Korea, Tsugaru, and Soya Straits. Inflow through the Tsushima/Korea Strait is divided into two separate inflow ports, one each for the western and eastern channels of the strait. Consistent with observations (see Preller and Hogan, 1998), the mean volume transport of the inflow is 2.0 Sv ($Sv = 10^6\,m^3/s$), but a seasonal signal is superimposed such that the maximum inflow and outflow of 2.66 Sv occur in July and the minimum of 1.34 Sv occurs in January (33% peak deviation from the mean). The inflow is consistently segmented so that 75% enters through the western channel and 25% through the eastern channel. Vertically, two-thirds of the inflow (for both channels) enter the basin through layer 1, while the remaining one-third enters through layer 2. The straits are closed in layers 3 and 4. Inflow through the Tsushima/ Korea Strait is exactly balanced by outflow through the Tsugaru and Soya straits using a modified Orlanski (1976) boundary condition. The outflow is distributed such that two-thirds of the flow exit through Tsugaru Strait and the remaining one-third through Soya Strait. The vertical distribution for the outflow is the same as for the inflow. HH2000 contains a detailed description of

the circulation dynamics, including the coupling of the abyssal and surface circulation and the impact of bottom topography. It also includes a complete description of the JES model configuration used here.

## 3. The atmospheric forcing products

The surface wind stress is the primary source of momentum flux into the ocean and the primary forcing of the upper-ocean circulation. Ocean circulation models, therefore, rely on the surface wind-stress (primitive equation models) or its curl (quasi-geostrophic models) as a specified surface boundary condition. In particular, the curl of the wind stress, which is important dynamically because it is a source of vorticity, is the principal forcing mechanism for the wind-driven circulation. In NLOM, the wind forcing is input via wind-stress and prescribed as a body force acting only on the layer in direct contact with the atmosphere, although the top layer responds to the curl through Ekman dynamics and the Sverdrup relation.

There are several different sources of wind-stress data sets, ranging from climatologies formed via statistical analyses of marine wind observations to those formed by data-assimilative operational atmospheric models. Hence these wind-stress data sets can be significantly different from each other and subject to several possible sources of error. Those constructed from historical records of marine observations are particularly vulnerable to errors based on the estimation of wind speed derived from ship observations at sea and the parameterization of the surface momentum flux by a bulk aerodynamic formula. Model-based data sets also are influenced by grid resolution, model physics, data assimilation methods, and first-guess errors. One shortcoming both wind-forcing data sources share is the native horizontal grid resolution, which is typically much larger than the internal radius of deformation for the ocean. This is particularly exacerbated in the JES, where some data sets with relatively coarse resolution ($2.5°$ for example) may have only a few grid points over the JES. As expected, OGCM response can be quite
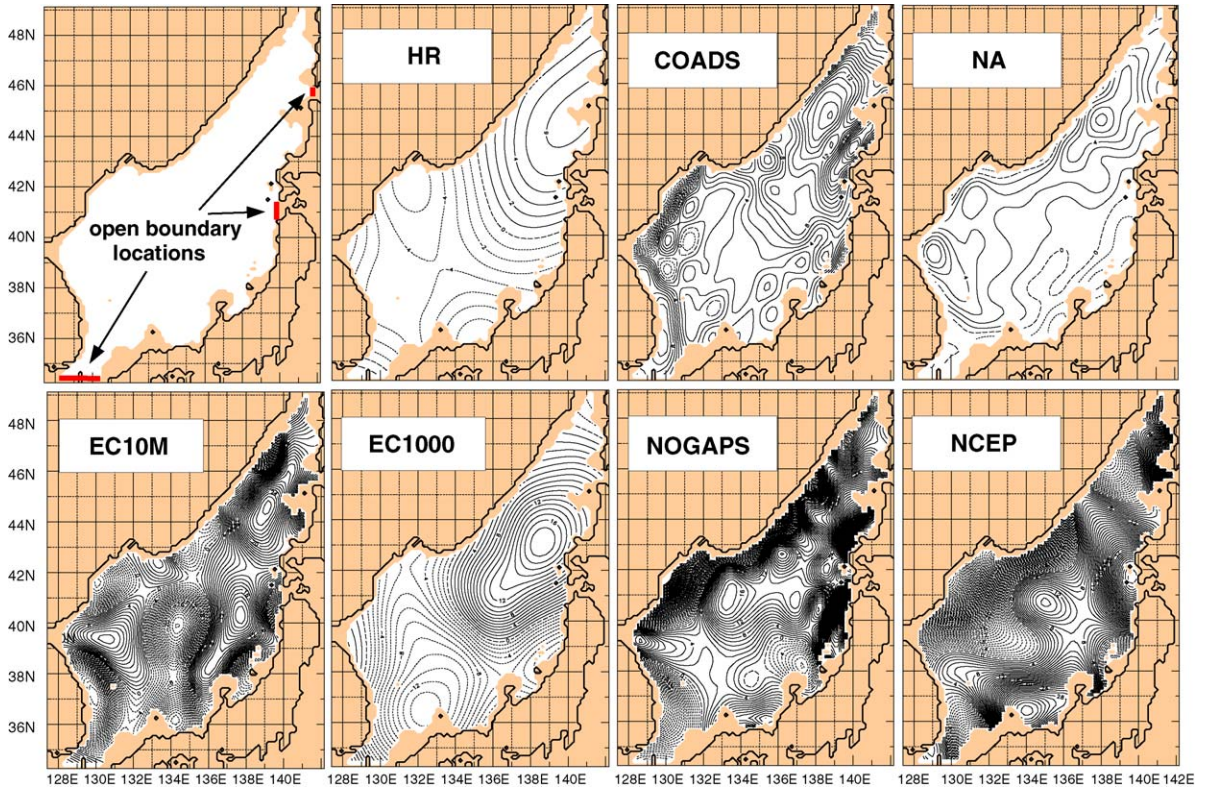
Fig. 2. Location map of open boundaries and annual mean wind-stress curl in $10^8$ Pa/M for the seven different wind-forcing data sets used in the study. Labels indicate which product is depicted.

different depending on which wind-forcing data set is employed. The object of this paper is to examine and quantify the differences in JES simulations that arise from forcing an ocean model with seven different wind-forcing data sets, which are described below and depicted in Fig. 2.

The Hellerman and Rosenstein (1983) (HR, hereafter) monthly mean wind-stress climatology has been widely used to force global and regional OGCMs. This climatology is comprised of 106 years of surface marine data, from 1870 through 1976, derived using a bulk aerodynamic formula, the World Meterological Organization (WMO) Beaufort equivalent scale for wind speed, and parameterizations similar to Bunker (1976). The native grid resolution is $2° \times 2°$. The wind stress was smoothed with one pass of a nine-point smoother to eliminate a two-grid interval noise that otherwise gives a noodling pattern in the wind

stress curl when the HR wind stress is interpolated to the $1/8°$ model grid. After the smoothing the annual mean wind-stress curl (Fig. 2b) shows little small-scale structure, and is characterized by positive (negative) wind-stress curl in the northeastern (southwestern) part of the basin.

da Silva et al. (1994a, b) developed a new Beaufort equivalent scale that they utilized to improve the estimated wind speeds of each observation (mostly wind estimates over 1945–89) in the COADS. Hence, this data set is different from that originally described by Woodruf et al. (1987). The new analysis also used higher resolution ($1° \times 1°$ globally excluding Antarctica) and a stability-dependent value for the drag coefficient ($C_D$).

Na et al. (1992, 1999) calculated sea-surface winds (at 10 m above sea level) twice daily for an 18-year period (1978–95) utilizing the Cardone (1969) model and twice-daily weather maps

published by the Japan Meteorological Agency. A bulk formula was used to calculate the wind-stress using the drag coefficient described by Garratt (1977). From this, monthly mean wind-stress and wind-stress curl were calculated over the East Asian Seas region with $0.5° \times 0.5°$ resolution. In the JES region, the annual mean wind-stress curl (Fig. 2d) is characterized by positive wind-stress curl in the northern part of the basin with local positive maxima near Vladivostok and the East Korea Bay, while negative curl is present in the southeastern part of the basin along the coast of Honshu.

The European Centre for Medium-Range Weather Forecasts (ECMWF) routinely performs global operational atmospheric nowcasts using a data-assimilative atmospheric model. An ECMWF re-analysis of archived data was used to form two monthly wind-stress climatologies, one based on the 10 m winds (EC10M, hereafter) and the other based on the 1000 mb winds (EC1000, hereafter). The ECMWF reanalysis was performed at 6-hourly intervals over 1979–93, using a fixed 1994 version of the ECMWF operational forecast model and data assimilation scheme (Gibson et al., 1997). The reanalyses have the advantage over the archived operational winds in that observations not available in the original nowcasts are included, and the entire time series is free of spurious variations associated with real-time changes in the operational model and data assimilation scheme (although changes in the data stream remain). The resolution of the EC10M winds was spectral T106/N80 Gaussian output on a $1.125°$ grid (lat. × long.), but the EC1000 winds were output on a $2.5° \times 2.5°$ grid after truncation to T47. There are significant differences in the resulting wind-stress curl fields (Figs. 2e–f), which are due in part to the difference in horizontal grid resolution. The EC10M curl shows much finer scale structure depicting alternating areas of positive and negative curl, whereas the EC1000 curl basically shows positive (negative) values in the northeastern (southwestern) part of the basin.

A monthly mean climatology of surface stresses covering July 1990–June 1997 was created using archived global operational atmospheric model nowcasts from the Fleet Numerical Meteorology

and Oceanography Center's Navy Operational Global Atmospheric Prediction System (NO-GAPS) (Hogan and Rosmond, 1991). The grid resolution of these analyses is $1.25° \times 1.25°$. This wind forcing is characterized by rich structure and strong gradients in wind-stress curl (Fig. 2(g) with overall positive curl in the north-central and eastern part of the basin and negative curl along the western side of the basin, except that the latter is bisected by a corridor of positive curl near the East Korea Bight.

Six-hourly surface wind-stresses over 1979–95 from a reanalysis performed with the National Centers for Environmental Prediction (NCEP) atmospheric model and data assimilation system were used to create the final monthly climatology used here. It is an improvement over the NCEP operational nowcast product for reasons similar to the case of ECMWF, including more atmospheric observations (Kalnay et al., 1996). The analysis was computed at spectral T62 and subsequently transformed to a $2.5° \times 2.5°$ grid. In the NCEP re-analysis, the surface wind-stress was computed using a drag coefficient that is a function of the bulk Richardson number (Townsend et al., 2000). Although this data set has relatively coarse resolution, the wind-stress curl depicts small-scale structure with significant variation in magnitude (note from Fig. 3 that this data set has the second highest basin-averaged wind energy). The overall pattern is characterized by positive (negative) curl in the eastern (western) part of the basin.

All of the wind-forcing data sets exhibit monsoonal seasonality, with weak winds from the southeast in summer and strong winds from the northwest in winter, although significant local variations in the strength and pattern of wind-stress and wind-stress curl are present. During wintertime, the mean synoptic-scale weather patterns are dominated by the Siberian high, which produces north and northwest winds traveling from the Asian continent over the JES, often in the form of cold-air outbreaks. The seasonality in the wind-forcing is reflected in the seasonal signal of wind energy in all of the wind-forcing products (Fig. 3). The wind energy is computed as the root mean square of $\tau_x$ and $\tau_y$. On average, Fig. 3 shows that the NOGAPS forcing has the strongest

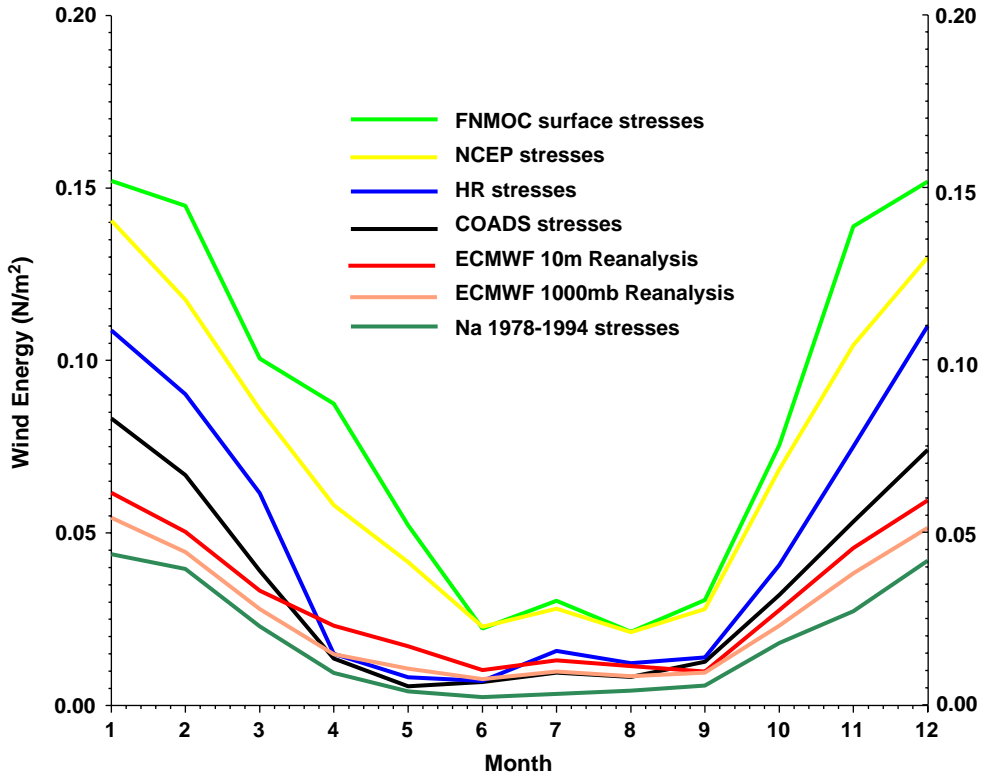Fig. 3. The annual cycle of the wind energy in N/m² averaged per month over the JES computational domain for the seven different wind-forcing data sets. See key for explanation.

basin-wide wind energy, while Na has the lowest. In general, this is consistent with the magnitude of the wind-stress curl values (Fig. 2), although some data sets contain relatively low values of wind energy (such as EC10 M and EC1000), but have relatively high magnitudes of curl and gradients of curl.

## 4. Linear response to the wind-forcing products

The linear solutions produced from a variety of wind sets provide a clear lowest-order response to the wind-stress forcing. As such, these solutions provide insight into the dynamics of observed circulation features as well as insight into nonlinear model response to the choice of wind-forcing product.

Following the approach of HH2000, the linear response to each of the atmospheric forcing data sets was calculated using a 1.5-layer reduced gravity model. These simulations represent the lowest-order dynamics as they have one internal vertical mode and a bottom layer that is infinitely deep and at rest. For these simulations, linearity was achieved by reducing the amplitude of the wind and straits forcing by a factor of $10^3$. This has the same effect as excluding the nonlinear terms in the governing equations without having to change the ocean model source code. HH2000 examined the linear response due to HR wind and straits forcing both separately and collectively, but here all the simulations include the straits forcing. The linear simulations are characterized by very small local-time derivatives, small nonlinear advective terms, and small-amplitude variations in
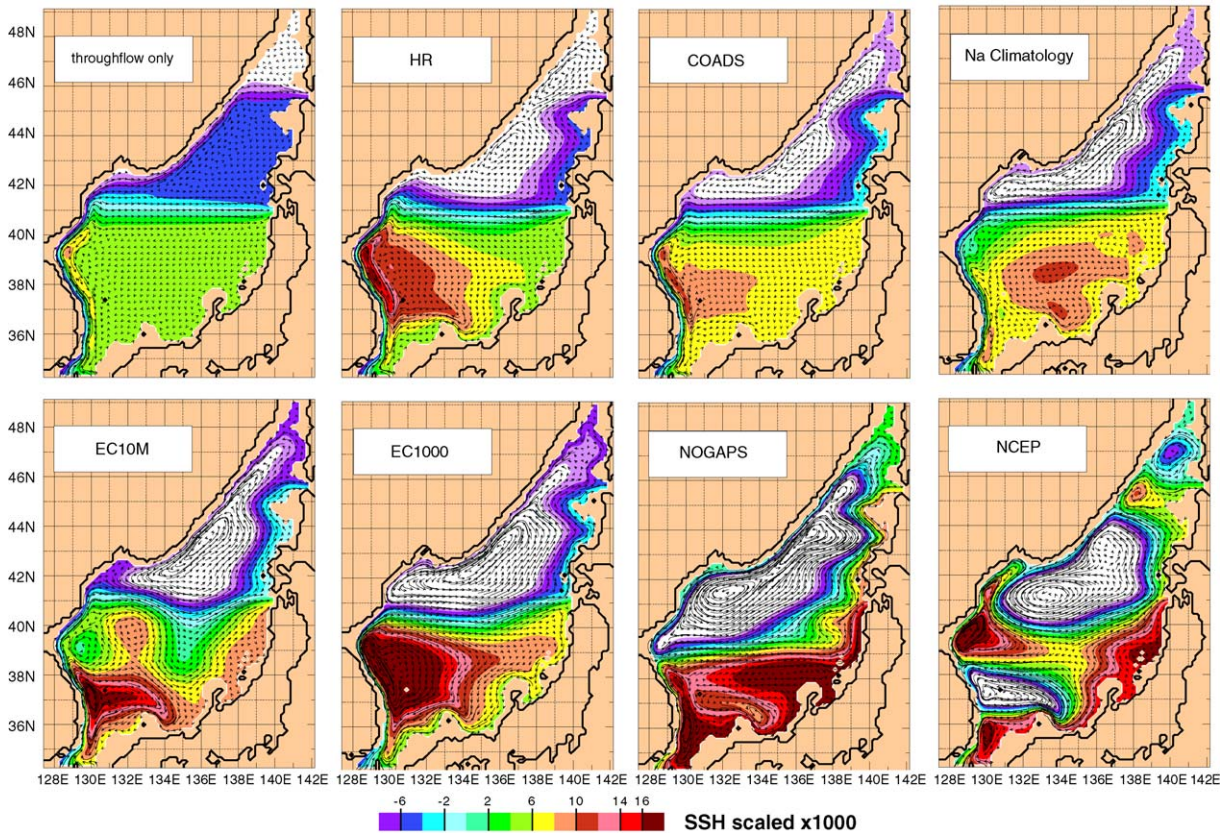
Fig. 4. Mean SSH and currents from the linear solutions forced by (A) throughflow only, throughflow and monthly wind-stress forcing by (B) HR, (C) COADS, (D) NA, (E) EC10M, (F) EC1000, (G) NOGAPS, (H) NCEP. The solutions were linearized by reducing the amplitude of the throughflow and wind forcing by $10^3$.

the interface depth. Thus, the possibility of diapycnal mixing is excluded.

Fig. 4 shows the annual mean SSH and currents from eight 1.5-layer, reduced-gravity simulations forced with different monthly mean wind-forcing products, except for Fig. 4a, which is forced only with flow through the straits (with the amplitude reduced by $10^3$). Dynamically, all of the linear solutions in Fig. 4 are essentially the same as Munk (1950), with a Sverdrup (1947) interior calculated using realistic wind and throughflow forcing and coastline geometry. However, in these simulations horizontal friction ($A = 50\,\text{m}^2/\text{s}$) is applied everywhere and the SSH field includes a component that balances the wind-stress and allows departures from constant SSH along the boundary (even where there is no flow through the boundary), but this component does not contribute to the velocity field.

Fig. 4a depicts the linear response to the throughflow forcing only, and as such serves as a baseline simulation for comparison to those that include the different wind-forcing data sets. Although it is uncommon to consider a model result driven by open-boundary conditions (only) in the context of Sverdrup dynamics, those dynamics are still valid, and in this case the TWC is manifested as a Munk ($\beta^{1/3}$) boundary layer that hugs the western boundary until it is forced to separate from the coast of Korea and flow eastward to satisfy the constraints of flow out of the Tsugaru and Soya Straits. That is why these zonal flows separate from the coast at the latitude of the straits, with two-thirds of the flow exiting

through Tsugaru and the remaining one-third through Soya (a distribution that is consistent with the open boundary configuration described in Section 2). The grossest deficiency in this solution is the northward flow along the Siberian coast (opposite to what is observed) and the lack of any flow to the northeast along the coast of Honshu. As described in HH2000, the resulting SSH patterns from the simulations forced with different wind climatologies are a linear superposition of the throughflow-driven solution (Fig. 4a) and the solution produced by wind forcing only (see Fig. 3 in HH2000).

The mean SSH shown in Fig. 4b–h is the linear solution for the simulations forced with HR, COADS, Na, EC10m, EC1000, NOGAPS, and NCEP, respectively, where the abbreviations are defined in Section 3. The most prominent difference between Fig. 4a and Fig. 4b–h is the presence of cyclonic circulation north of the subpolar front, consistent with observations. This suggests that the LCC is a predominantly wind-driven current that can exist in the absence of buoyancy effects. All show a Munk ($\beta^{1/3}$) boundary layer that hugs the western boundary east of Korea except for the case forced with NCEP, which produces the most unrealistic flow patterns of all the wind sets. All simulations that include wind forcing except the NCEP-forced simulation also show an unrealistic southwestward return flow along at least part of the Honshu north coast.

## 5. Nonlinear response to the wind-forcing products

The linear simulations forced with winds and throughflow discussed in the previous section demonstrated that many of the large-scale circulation features in the JES could be grossly reproduced with minimal dynamical ingredients when the model is forced with winds and throughflow. In particular, all simulated the cyclonic circulation of the subpolar gyre, but most had unrealistic southwestward flow along the coast of Honshu. In the following section, the model sensitivity to the different wind-forcing data sets is examined in simulations with more complexity. The changes include nonlinearity, the addition of bottom

topography, multiple internal modes, diapycnal mixing, and ventilation of layer interfaces. These additions allow the possibility of barotropic/baroclinic flow instabilities, the formation of inertial boundary layers and jets, and isopycnal outcropping.

Fig. 5a shows the mean SSH for the simulation with straits throughflow forcing only, and Figs. 5b–h show the mean SSH from the simulations forced with the seven different monthly wind-stress climatologies in addition to straits throughflow. The case forced with straits throughflow only (Fig. 5a) is able to simulate almost all of the major current systems remarkably well, the exception(s) being the NKCC and the unrealistic "overshoot" of the EKWC. Although some observations (Shin et al., 2001; Suh et al., 1999) suggest the presence of a warm eddy in the East Korea Bay, it is unclear if this eddy is formed locally by wind stress curl, or as a pinched-off eddy of the EKWC, or by trapped cold water surrounded by a migrating warm filament associated with the warmer EKWC water, or some other mechanism. In this paper, overshoot of the EKWC is when the mean EKWC flows northward continuously along the Korean coast past ~40°N. It is noteworthy that the straits-forced only simulation reproduces two major circulation features not seen in the linear simulation (Fig. 4a). One is the southward-flowing LCC and the overall cyclonic flow of the subpolar gyre (albeit weakly) in the absence of *any* wind forcing, as these features are believed to be connected with the wind-driven circulation in the JES. In this case, they are associated with a weak nonlinear recirculation gyre. The second feature is the northeastward-flowing NB of the TWC along the north coast of Honshu. In this simulation, the NB is driven entirely by isopycnal outcropping as discussed in HH2000. This is the case for all of the nonlinear simulations in Fig. 5, where the corresponding linear simulation shows no wind-driven contribution to the NB, i.e. the simulations forced by throughflow only and throughflow plus HR, COADS, Na, and EC1000.

The dynamics of the linear and nonlinear $1/8°$ simulations forced by throughflow only and throughflow plus HR are discussed extensively in
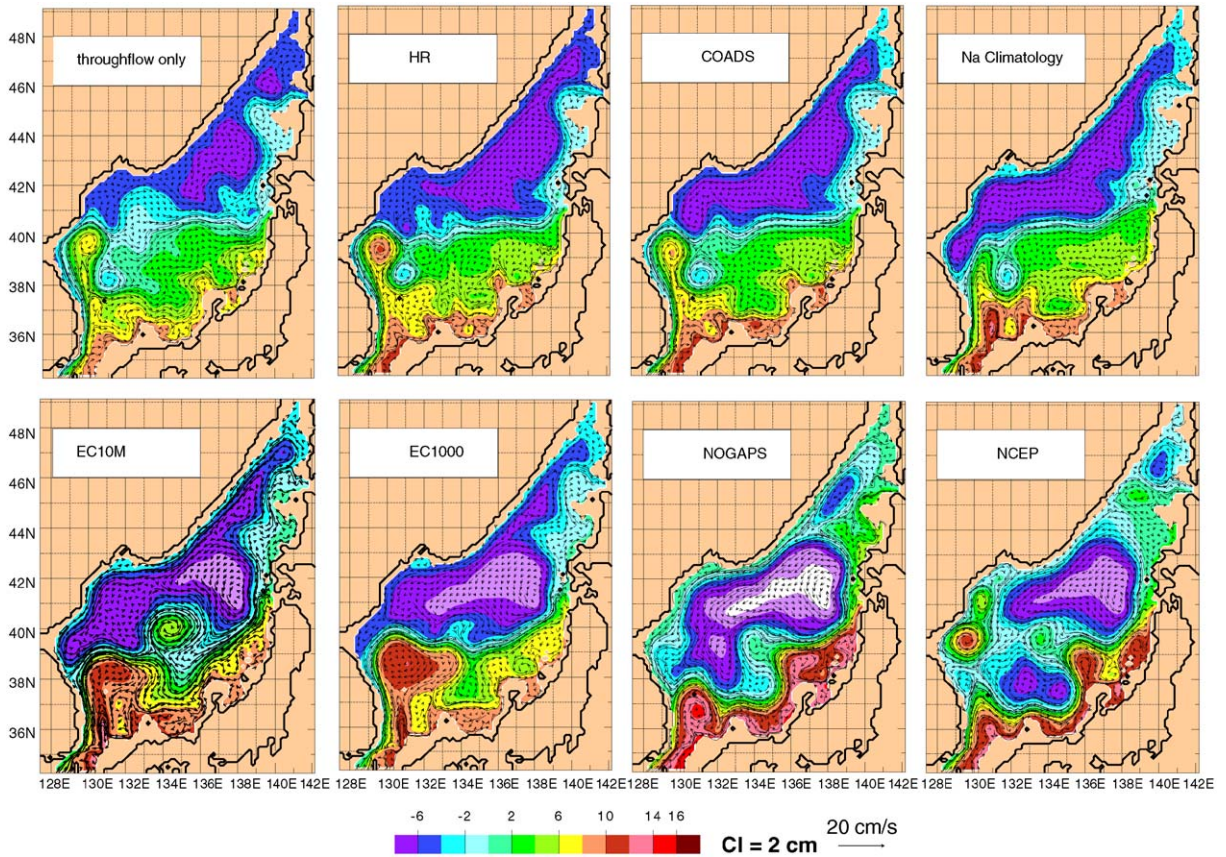
Fig. 5. Mean SSH (color) and currents (vectors) from four-layer $1/8°$ nonlinear simulations forced by (A) throughflow only, throughflow and monthly wind-stress forcing by (B) HR, (C) COADS, (D) NA, (E) EC10M, (F) EC1000, (G) NOGAPS, (H) NCEP. Contour interval is 1 cm.

HH2000. With these forcings, both the linear and nonlinear $1/8°$ simulations show overshoot of the EKWC separation from the Korean Coast. HH2000 also discuss the $1/8°$ nonlinear simulation forced by throughflow plus EC10M which shows realistic EKWC separation, but not a corresponding linear simulation. Thus, they did not consider the substantial role that the NB may play in EKWC separation, a topic discussed shortly.

Figs. 5b and c show the mean SSH from the simulations forced with the HR and COADS monthly wind climatologies, respectively. In these simulations the mean SSH is quite similar to that shown in Fig. 5a, except that the strength of the subpolar gyre is enhanced because of positive wind-stress curl in that region. However, the EKWC still overshoots the observed separation latitude at $1/8°$ resolution because of negative or relatively weak positive wind-stress curl in the western subpolar gyre region (Fig. 2b–c). In contrast, the mean SSH from the simulation with atmospheric forcing from the Na monthly wind-stress climatology is shown in Fig. 5d. In this simulation, the LCC continues southward as the NKCC until its confluence with the EKWC at about 38°N, consistent with the observed separation latitude of the EKWC. Also consistent with the observations, part of the EKWC flow continues eastward along the subpolar front, but some recirculates to the south before flowing northeastward along the coast of Honshu. Models forced with this wind set (Seung, 1992; Seung

and Kim, 1993; Kim and Yoon, 1996, 1999), including those with relatively coarse horizontal grid resolution, tend to show the EKWC leaving the coast near the observed separation latitude (although some may include additional dynamics or forcing terms such as buoyancy forcing). This is due to a local maximum in the amplitude of positive wind-stress curl near East Korea Bay and the large area of positive wind-stress curl in the northern region of the basin (Fig. 2d), even though the total wind energy is the lowest of all the wind-forcing data sets examined (Fig. 3). In the linear simulation with Na wind forcing, note that the EKWC bifurcates into a wind forced branch that leaves the coast between 38° and 39°N and a throughflow forced branch that overshoots and separates near 41°N (Fig. 4d). In the nonlinear solution, part of the flow required to feed the outflow straits is diverted into the NB, making it easier for the wind-stress curl to dominate in determining the EKWC separation latitude (Fig. 5d). A similar situation exists for the EC10M linear and nonlinear simulations.

Figs. 5e and f show the mean SSH from the nonlinear simulations forced with the monthly climatologies formed from the ECMWF re-analysis (10 m and 1000 mb, respectively). Recall that the EC10M winds have 1.125° resolution and EC1000 have 2.5° resolution. Here we assume the primary differences in the structure, magnitude and gradients of the wind-stress curl in the EC1000 data set are due to truncation of the spectral grid to T47 (and subsequent interpolation to a 2.5° × 2.5° Mercator grid). A notable feature in the EC10M data set is the zonal corridor of positive wind-stress curl extending eastward from East Korea Bay at 39°N (which is also seen in the NOGAPS and Na wind-stress curl patterns ( Figs. 2d–e,g)). As a result, the mean separation latitude of the EKWC is farther to the south in the simulation forced with EC10M (Fig. 5e) than the Na-forced simulation.

Another significant feature of the EC10M mean wind-stress curl is the strong region of negative wind-stress curl in the central JES centered near 40°N, 134°E flanked by regions of strong positive wind-stress curl with a band of strong negative wind-stress curl along the eastern boundary in the

corresponding latitude range. This results in a pattern of large meanders across the basin between 38°N and 40°N in the linear simulation (Fig. 4e). These are not seen in any of the other simulations, including EC1000. A similar pattern of meanders is seen in the nonlinear simulation, but with the northward meander in the central basin shifted eastward 2° so that it lies over the Yamato Rise. This eastward shift is due to the mean abyssal flow along the geostrophic contours of the topography. The role of abyssal currents in steering upper currents is discussed in Section 6. Another significant difference between the linear and nonlinear simulations with EC10M wind forcing is seen in the pathway of the subpolar front, a dual pathway in the linear simulation (the meandering pathway and a more zonal pathway along 41°N) and only the meandering pathway in the nonlinear simulation. This is a consequence of the dynamics used in explaining EKWC separation from the coast in the nonlinear Na simulation (Fig. 5d), where much of the flow connecting the inflow and outflow ports is shifted to the NB.

In marked contrast to EC10M, the EC1000 wind-stress curl is very smooth and dominated by positive wind-stress curl in the northeast half of the basin and negative in the southwestern half. Gone is the region of strong positive wind-stress curl east of East Korean Bay that played a key role in EKWC separation, but a remnant of positive wind-stress curl remains in East Korea Bay. Also gone is most of the meandering in the subpolar frontal region of the linear and nonlinear simulations with EC1000 wind forcing, including the northward meander and gyre above the Yamato Rise. However, the anticyclonic gyre east of Korea is the strongest of all of the simulations. The linear simulation shows a single EKWC pathway that leaves the coast between 40°N and 41°N. There is no bifurcation into the wind-driven and through-flow-driven pathways as seen with Na and EC10M wind forcing. Yet, the nonlinear simulation shows partial separation of the EKWC starting at 38°N and complete separation by 38.8°N. Here we investigate the hypothesis that this separation is inertial and can be described by a constant absolute vorticity (CAV) trajectory at least to the northernmost latitude of the mean EKWC

trajectory after separation. In addition, the positive wind-stress curl in East Korea Bay and anticyclonic abyssal flow around the rise near the separation point may have some influence on the pathway after separation. HH2000 found that flow around this rise could play a key role in EKWC separation from the coast. Of the simulations in Fig. 5, the simulation using EC1000 wind forcing has the strongest flow around this rise with a maximum greater than 1 cm/s near 129.5°E, 38.2°N, but still much weaker than in simulations where this had an effect in HH2000.

A CAV trajectory occurs in a special case where conservation of potential vorticity reduces to CAV. It occurs at the core of a steady, geostrophic, inviscid current (no vorticity due to shear). In a 1.5-layer nonlinear reduced-gravity model on a β-plane, it forms a streamline with constant speed along a constant layer thickness contour. Starting at an inflection point in the trajectory, the maximum northward penetration of a CAV trajectory is given by

$$b = d \sin \tfrac{1}{2}\Theta_0, \qquad (1)$$

where

$$d = 2\left(V_c/\beta\right)^{1/2} \sin 1/2\Theta_0 \qquad (2)$$

and $V_c$ is the speed at the core of the current, $\beta = df/dy$, and $\Theta_0$ is the angle of the flow at the inflection point measured counterclockwise from due east (Hurlburt and Thompson, 1982). Of the eight JES simulations shown in Fig. 5, the simulations with EC10M and EC1000 wind forcing have the strongest EKWC at the separation point with $V_c = 36$ cm/s in the top layer and are the two where CAV trajectory theory may be most useful and applicable. However, at the northernmost point of the trajectory, $V_c$ drops to 23 cm/s in the simulation using EC10M and 25 cm/s in the simulation using EC1000. Hence, we choose to specify the other parameters and solve for

$$V_c = \beta b^2 / 4 \left( \sin \frac{1}{2}\Theta_0 \right)^2. \qquad (3)$$

It is also difficult to precisely determine the latitude of the inflection point, a potential source of significant error, since it is used in calculating

$b^2$. We used the separation latitude (37.25°N), $\beta = 1.77 \times 10^{-11}$ m$^{-1}$ s$^{-1}$ at 38°N, and $\Theta_0 = 104.6°$ (106.5°) to obtain $b = 233$ km (272 km) from the simulations and $V_c = 38$ cm/s (51 cm/s) from Eq. (3) for the simulations using EC10M (EC1000). The values of $V_c$ obtained from CAV trajectory theory are obviously higher than in the numerical simulations, particularly for the simulation using EC1000. Continuation of some frictional contact of the current with the boundary layer after separation, more strongly in the simulation using EC1000, is an explanation that is consistent with these results. Still, the results indicate that the CAV dynamics are a useful benchmark in assessing the deviation from their prediction, as will be seen in Section 6.

NOGAPS and NCEP are the strongest wind-forcing products and tend to dominate over the throughflow forcing in the model simulations (Fig. 2). The NCEP pattern of mean wind-stress curl is largely the opposite of Na (and much stronger) with negative wind-stress curl over the northwestern half of the basin and positive in the southeastern half. The simulations forced with the NOGAPS wind stresses (Fig. 5g) and the NCEP reanalysis (Fig. 5h) are characterized by strong cyclonic flow over a large part of the JES basin. The pattern and magnitude of the wind-stress curl in these two data sets result in strong Ekman suction in the subpolar gyre, enhancing its strength. In fact, in both of these simulations the subpolar front exists only to the extent that it forms the southern boundary of the subpolar gyre. Accordingly, the NB is stronger in these two solutions than in any of the others. Indeed, one could argue that these simulations reproduce the separation of the EKWC from the Korean coast and northward flow along the coast of Honshu reasonably well. A more detailed discussion of the EKWC and the current pathway after separation from the coast, in relation to the 1/32° simulations using these two wind-forcing products, is contained in Section 6. However, other aspects of these solutions, particularly the double gyre cyclonic circulation feature near 133°E, 38°N and the strong anticyclonic eddy near the East Korea Bay in Fig. 5h are less realistic. These two features are due to the region of strong positive wind-stress

curl in the southernmost JES and strong negative wind-stress curl east of East Korea Bay, respectively, in the NCEP forcing (Fig. 2h).

Although the wind stress used by NLOM acts only on the layer in direct contact with the atmosphere, the mean abyssal circulation is also affected by the surface wind forcing, in that wind forcing data sets with stronger wind-stress and positive wind-stress curl (e.g. Figs. 2 and 3) tend to promote more isopycnal outcropping and thus more vigorous diapycnal mixing and exchange between the surface and subsurface layers, including the abyssal layer. This is reflected in maps of abyssal-layer kinetic energy of the mean flow (KEM) as shown in Fig. 6. As such, the simulation forced with NOGAPS, which has the strongest

positive wind-stress curl with a relatively large zonal extent, has a relatively strong cyclonic mean abyssal circulation (Fig. 6g). This is consistent with limited but recent observations, which suggest deep cyclonic flow in the JES, but with more episodic events (rather than mean) of the magnitude seen in Fig. 6g (Takematsu et al., 1999; Senjyu et al., 2002). Conversely, the cases forced with EC1000, EC10m, and NCEP show weaker cyclonic abyssal circulation, and the cases forced with HR, COADS, and inflow/outflow only have weakly anticyclonic abyssal circulation. The relatively strong mean abyssal circulation in the $1/8°$-NOGAPS-forced simulation is driven by relatively strong vertical mixing in the subpolar gyre, where there is isopycnal outcropping. This is different
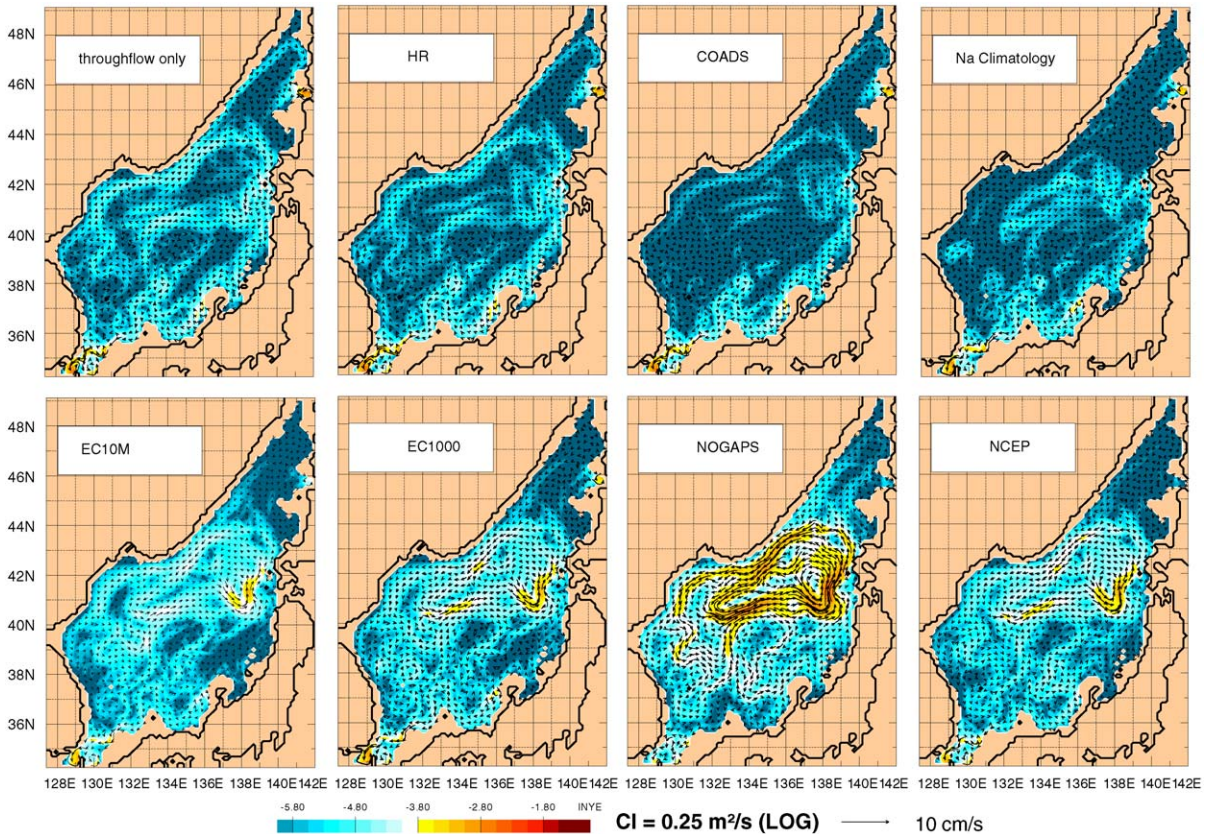


Fig. 6. Kinetic energy per unit mass of the mean abyssal flow (color) and mean abyssal currents (vectors) for the $1/8°$ simulations shown in Fig. 5: (A) throughflow only, throughflow and monthly wind-stress forcing by (B) HR, (C) COADS, (D) NA, (E) EC10M, (F) EC1000, (G) NOGAPS, (H) NCEP.

from the mixed barotropic/baroclinic instability mechanism described in HH2000 that energizes the abyssal layer, but the result is basically the same. Both depict robust abyssal-layer currents that are topographically constrained and influence the pathways of surface-layer currents via upper ocean–topographical coupling, including an influence on the separation latitude of the EKWC in some cases.

The location of diapycnal mixing between the surface and abyssal layers helps to elucidate the location and process of deep-water formation and abyssal-layer current pathways. As described in HH2000, in NLOM outcropped layers do not attain zero-layer thickness, but rather outcrop to a specified layer thickness that controls activation of vertical mixing. The location where the layer(s) outcrop is co-located with the location of the

interfaces ventilating. HH2000 describe the ventilation patterns for the 1/8° case forced with the HR monthly wind climatology, inflow/outflow through the straits (no wind forcing), and both as a function of the fraction of time that a given interface ventilates. Those calculations have been extended to the simulations discussed here for the deepest (third) interface (Fig. 7). In all simulations the deepest interface ventilates north of the subpolar front but the areal extent varies significantly, and in all cases the location where the bottom interface is ventilating is largely co-located with the pattern of positive wind-stress curl. The positive wind-stress curl invokes vigorous Ekman suction, causing the isopycnals to dome upward and outcrop once the specified minimum layer thickness is reached. Likely regions of intermediate and deep-water formation are located where the
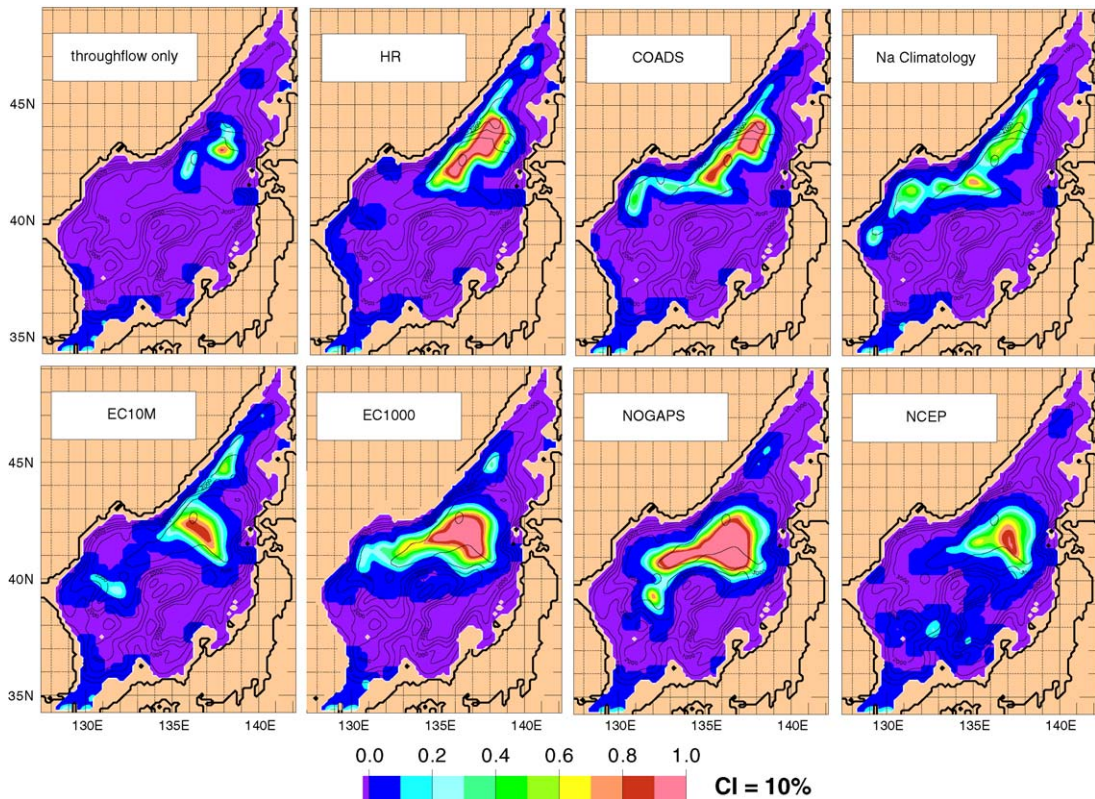


Fig. 7. Maps of the percent of time that the third (bottom) interface ventilates for the 1/8° throughflow only and seven different wind climatology (including throughflow) cases. Units are percent of time; contour interval is 10%. Note that 0% is a separate color.

bottom interface is ventilating most of the time. In all cases this is north of the subpolar front in the subpolar gyre. This is reasonable, and consistent with limited observations (e.g., Senjyu and Sudo, 1994; Seung and Yoon, 1995), but there are substantial differences in the outcropping patterns depicted in Fig. 7. Hence, when using a numerical model to investigate water-mass formation and movement, particular care should be given to the choice of atmospheric forcing.

## 6. Comparison of nonlinear model responses to the combined effects of wind-forcing choice and upper ocean–topographical coupling

As previously mentioned, the simulations described in Section 5 were run with $1/8°$ horizontal grid resolution to elucidate more clearly the impact of wind forcing rather than flow instabilities. This is not to say those simulations are devoid of flow instabilities, as they are eddy-resolving. However, HH2000 demonstrated that the flow instabilities are much more pervasive at $1/32°$ resolution, and that flow instabilities at that resolution have a profound impact on the surface and abyssal circulation when the model is forced with HR climatological winds and throughflow forcing. In particular, the stronger baroclinic instability transfers much greater eddy kinetic energy to the abyssal layer. This results in much stronger abyssal flow and much stronger upper ocean—topographical coupling via a mixed baroclinic/barotropic instability, where baroclinic instability is key to the coupling because of the strong downward energy transfer.

In this section we compare the mean surface (Fig. 8) and mean abyssal (Fig. 9) results from $1/32°$ JES simulations forced by six of the wind products. Simulations forced by COADS and throughflow only are omitted due to similarity of the $1/8°$ nonlinear simulations with the $1/8°$ HR-forced simulation. The six simulations are identically configured except for the wind forcing, and all include the throughflow. They are also configured identically to the corresponding $1/8°$ simulations, except for (1) the grid resolution (and corresponding improvements in resolving the

model boundary and bottom topography) and (2) the eddy viscosity, which was reduced from $A = 50\,m^2/s$ at $1/8°$ to $5\,m^2/s$ at $1/32°$.

Substantial impacts are seen in both the surface layer (Fig. 5 vs. Fig. 8) and the abyssal layer (Fig. 6 vs. Fig 9) due to the resolution increase (and associated eddy viscosity decrease) and the strong upper ocean–topographical coupling via baroclinic instability. Although the mean SSH of the simulations with the different wind forcings generally demonstrate increased similarity at $1/32°$ resolution, the choice of wind-forcing product retains a large impact. The mean surface-layer circulation from the $1/32°$ NOGAPS-forced simulation shows the least change from its $1/8°$ counterpart because the $1/8°$ simulation already had relatively strong abyssal flow that steered upper-ocean currents, including the pathway of the subpolar front in the vicinity of the Yamato Rise. That abyssal flow was due to greater isopycnal outcropping than in the other $1/8°$ simulations (as discussed in Section 5). However, the changes that did occur in the $1/32°$ NOGAPS-forced simulation improved it to the point that, unlike at $1/8°$ resolution, it is no longer an outlier in relation to the other $1/32°$ simulations (which have also converged toward the $1/32°$ NOGAPS-forced simulation). Only the NCEP-forced simulation remains a gross outlier at $1/32°$ resolution.

The $1/8°$ and $1/32°$ EC10M simulations also have relatively similar mean surface-layer circulation because the flow around the Yamato Rise is supported by a feature in the wind-stress curl in addition to influence by the Yamato Rise (as discussed in Section 5). All the $1/32°$ simulations, except for the NCEP-forced, show strong impact of the Yamato Rise on the pathway of the subpolar front, but, except for the EC10m simulation, this is entirely due to abyssal current steering of the surface-layer mean current. At $1/8°$ these abyssal currents were driven by vertical mixing due to isopycnal outcropping, but at $1/32°$ they are driven almost entirely by downward transfer of energy due to baroclinic instability, except for a significant contribution from vertical mixing in the NOGAPS-forced simulation (Fig. 6 vs. Fig. 9). The $1/32°$ NCEP-forced simulation does not show a Yamato Rise impact on the
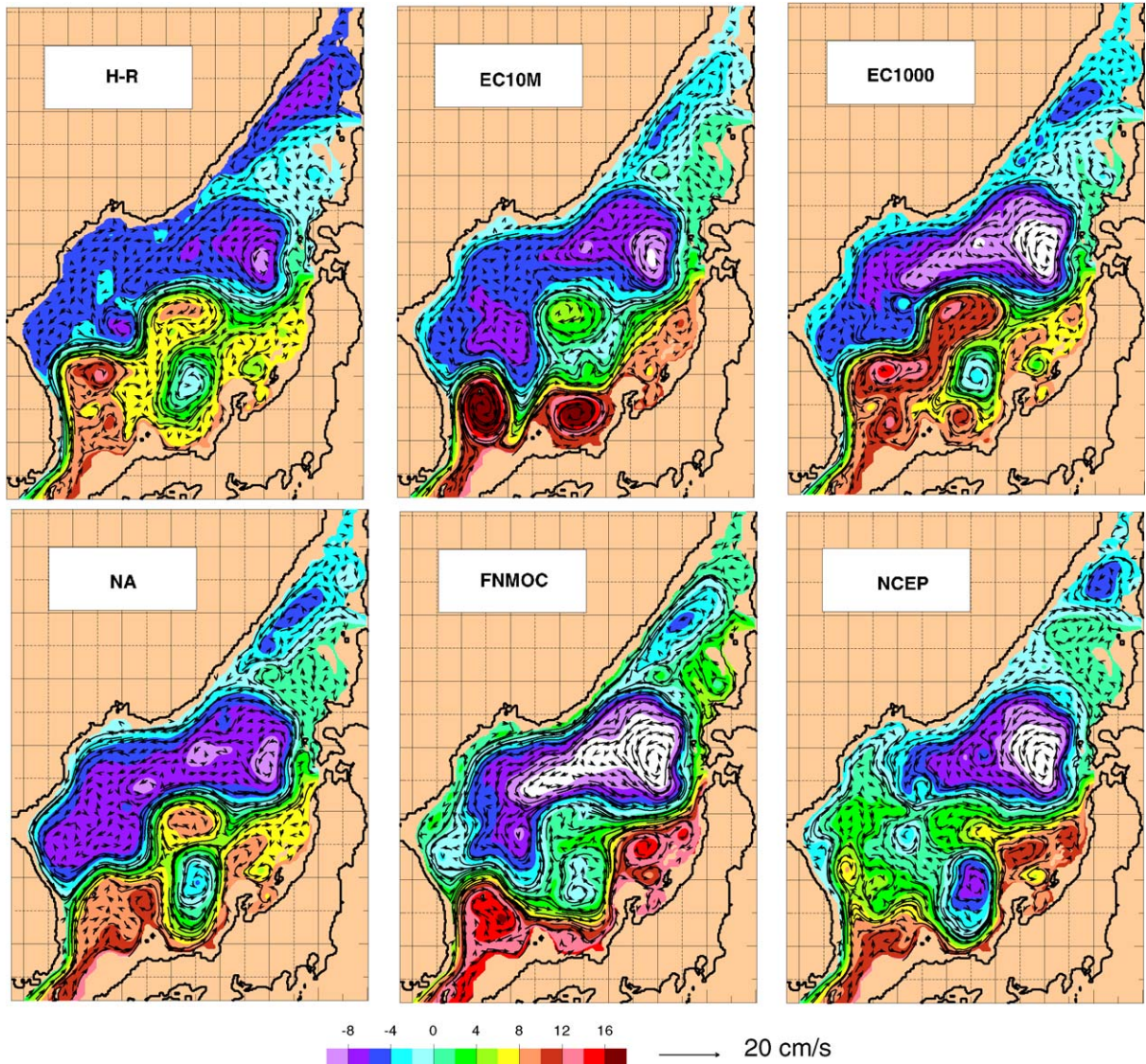
Fig. 8. Mean SSH (color) and currents (vectors) from four-layer $1/32°$ nonlinear simulations forced by (A) throughflow only, throughflow and monthly wind-stress forcing by (B) HR, (C) COADS, (D) NA, (E) EC10M, (F) EC1000, (G) NOGAPS, (H) NCEP. Contour interval is 1 cm.

subpolar frontal pathway because this front approaches the rise from the northwest and lacks a frontal segment between the EKWC and the west side of the Yamato Rise. The reasons for this are discussed shortly.

HH2000 showed that upper ocean–topographical coupling was essential for realistic simulation of the EKWC separation from the coast (when

forced with HR winds) and to prevent the overshoot of the observed separation latitude seen in the corresponding $1/8°$ simulation. They also demonstrated that anticyclonic abyssal flow around a rise centered at $38.3°$N, $129.8°$E was crucial to the separation. In addition, there is strong abyssal flow cyclonically around the rim of the abyssal plain at $\sim 2500$–$3000$ m depth (seen in
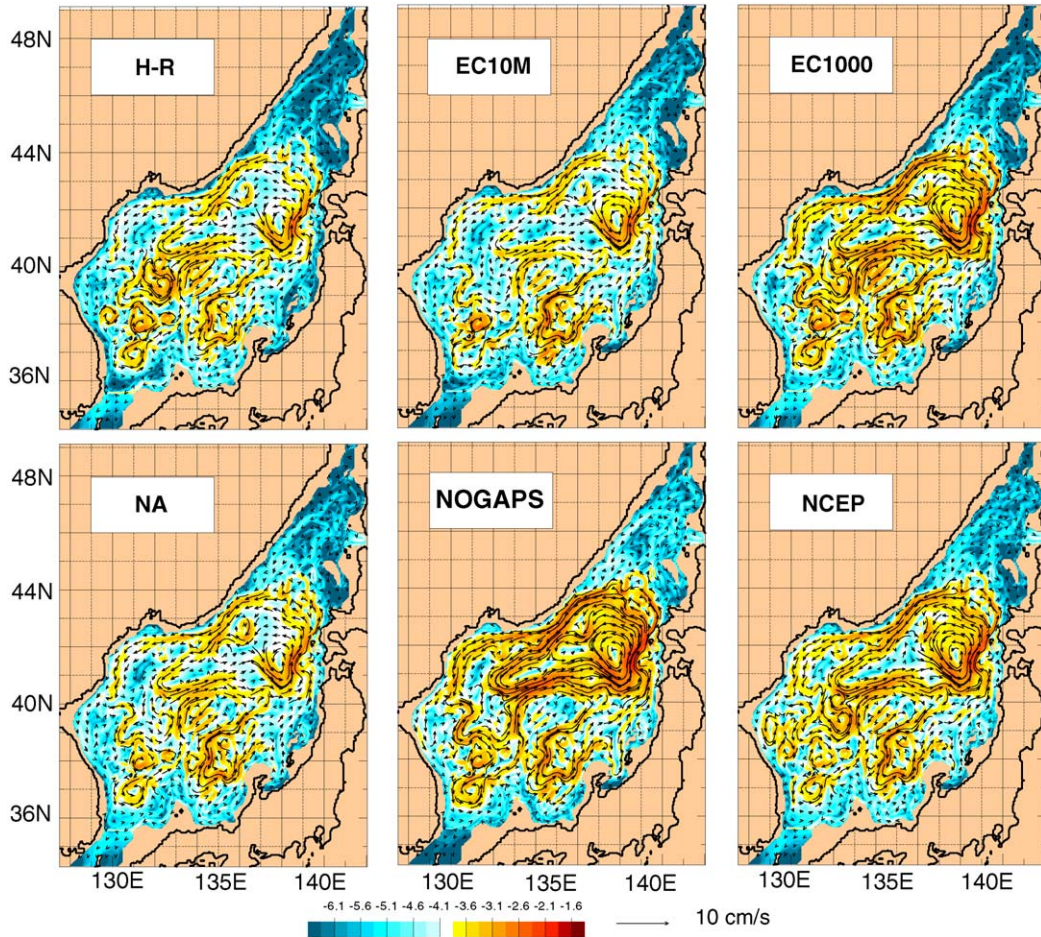
Fig. 9. Kinetic energy per unit mass of the mean abyssal flow (color) and mean abyssal currents (vectors) for the 1/32° simulations shown in Fig. 8: (A) throughflow only, throughflow and monthly wind-stress forcing by (B) HR, (C) COADS, (D) NA, (E) EC10M, (F) EC1000, (G) NOGAPS, (H) NCEP.

all the 1/32° simulations). This flow proceeds southward to a point immediately east of the rise that is crucial to EKWC separation and then abruptly changes to eastward flow along 38.5–38.8°N toward the Yamato Rise. After EKWC separation from the coast, the surface current proceeds eastward as the subpolar front and parallels this eastward abyssal current to the Yamato Rise. The same is seen in the 1/32° EC1000-forced simulation which has a surface flow pattern that is very similar to the 1/32° HR-forced simulation, but with generally larger amplitude.

The EC10M-, Na-, and NOGAPS-forced simulations all had realistic EKWC separation latitudes at 1/8° resolution due to the wind forcing, and that remains the case at 1/32° resolution. All three have post-separation pathways that pass southeast of the rise at 38.3°N, 129.8°E, and flow around this rise is less energized in these simulations. However, the northward penetration of all three pathways is limited to a lower latitude than in the HR- and EC1000-forced simulations because they approach the eastward abyssal current from the south and because of anticyclonic abyssal flow around a rise centered at 38.0°N,

133.3°E. In the Na-forced simulation, the eastward portion of the surface-current pathway lies along the southern side of the eastward abyssal current and north of the rise.

In the 1/8° and 1/32° NOGAPS- and 1/32° EC10M-forced simulations, the post-separation pathway forms a meander where the pathway returns toward the south after reaching maximum northward penetration. That pathway is nearly the same for the 1/8° and 1/32° NOGAPS-forced simulations. The EC10M-forced simulation, which equaled the EC1000-forced simulation in having the strongest EKWC at 1/8° resolution, has formed a circular nonlinear recirculation gyre at 1/32° resolution with a diameter of 200 km between speed maxima and with maximum mean speed in the EKWC increasing from 36 to >50 cm/s (the strongest of the 1/32° simulations). Other possible influences for change in the EKWC separation at 1/32° resolution are (1) a southward abyssal current adjacent to the western boundary, (2) a change in the surface-layer outcropping causing a change in the strength of the NB (discussed in Section 5), or a change in the subpolar gyre in the vicinity of separation, and (3) the strength of the EKWC. The maximum mean surface-layer speed of the EKWC in cm/s are for HR = 40, EC10M = 52, EC1000 = 43, Na = 24, NOGAPS = 29 and NCEP = 28. The results indicate that any influence of (1) or (2) is not large. The size/strength of the subpolar gyre does not show substantial changes at 1/32°, but for some simulations the southward NKCC does show increases in maximum mean surface-layer speed, ~25% with EC10M, 0% with EC1000, 70% with Na and 20% with NOGAPS forcing. At 1/32° the corresponding speeds of the NKCC (cm/s) are 3 with HR, 8 with EC10M, 6 with EC1000, 26 with Na, and 18 with NOGAPS forcing. There is no NKCC with NCEP forcing, just a small cyclonic gyre spanning 38–39°N. For all six simulations, the southward deep western boundary current shows obvious increases at 1/32° (Fig. 6 vs. Fig. 9). Despite the preceding changes, the EKWC separation does not change appreciably for the EC10M-, Na-, and NOGAPS-forced simulations. In addition, the NCEP-forced simulation still overshoots at

1/32° and the strength of the southward western boundary currents are not significant to the explanation for EKWC separation in the HR- and EC1000-forced simulations, as clearly demonstrated by HH2000 for the HR-forced simulation. Also, there is no relation between the strength of the EKWC and its latitude of separation or its post-separation pathway, except for some speed-related pathway modification in the EC10M simulation (which had the strongest EKWC).

For the 1/32° EC10M and the 1/8° and 1/32° NOGAPS-forced simulations, the pathway after separation was tested for agreement with a CAV trajectory using the methodology introduced in Section 5. For the 1/32° EC10M (1/32°, 1/8° NOGAPS)-forced simulations we used a separation latitude of 36.7°N, $\beta = 1.79 \times 10^{-11}\,\mathrm{m^{-1}\,s^{-1}}$ at 37°N and $\Theta_0 = 92.1°$ (93.1°, 90°) to obtain $b = 155$ (155, 122) km from the simulations and calculated $V_c = 21$ (20, 13) cm/s from Eq. (3). Since the simulated value of $V_c$ is a maximum of 52 (29, 26) cm/s and the minimum for $V_c$ anywhere in layers 1 or 2 between EKWC separation and its northernmost latitude is 33 (21, 15) cm/s, the pathway predicted by CAV trajectory dynamics would extend farther north (larger value of b) than simulated in these three cases, the opposite of the result obtained at 1/8° using EC10M forcing (Section 5).

The agreement with CAV trajectory theory for the 1/32° NOGAPS-forced simulation is relatively good, but that may not be due to CAV trajectory dynamics. Baroclinic instability is strong in the 1/32° simulations and can shorten the meander wavelength compared to a CAV trajectory. However, baroclinic instability is weak at 1/8° resolution, making this explanation inconsistent with the similarity between the 1/8° and 1/32° pathways in the NOGAPS-forced simulations. Further examination of the 1/32° NOGAPS-forced simulation (and the other two simulations) reveals that, after EKWC separation, the current is augmented by flow joining the eastward jet from the north via the NKCC and a second current (with a mean speed of ~11 cm/s in the 1/32° NOGAPS-forced simulation) merging near the northernmost point of

the mean meander after separation. The latter is strongly barotropic ($\sim$6 cm/s in the abyssal layer). In the abyssal layer, this is the same current that turns eastward and constrains the mean pathway in the $1/32°$ HR-, EC1000-, and Na-forced simulations. Here it would limit the northward meander penetration of the separated jet in the $1/32°$ NOGAPS- and EC10M-forced simulations, which have the same northward penetration. In the $1/8°$ NOGAPS-forced simulation, the northward penetration is insufficient to be limited by this abyssal current, which is present at 1–2 cm/s in that simulation.

Additional influence on the pathways of the $1/32°$ simulations comes from stronger anticyclonic abyssal flow around the rise centered near $38.0°$N, $133.3°$E ($<$1 cm/s in the $1/8°$ NOGAPS-forced simulation) and, in all three, southwestward abyssal flow entering the Ulleung basin via a deep channel on the east side of the rise. About one-half degree to the southeast of this deep channel compensating northeastward flow exits along the eastern side of the channel. This combination of abyssal flow steers an indentation in the southeastward surface jet in all three simulations. It is best seen in the $1/32°$ NOGAPS-forced simulation where it is centered near $37.6°$N, $131.9°$E (Fig. 9e) (a much larger indentation will be shown in Section 7). This abyssal steering also can limit the northward penetration of the surface current meander. Unlike the simulations forced by the other wind sets (except NCEP), the NOGAPS wind-stress curl strongly forces the current southward after EKWC separation in the linear simulation (Fig. 4g) and therefore can also play a major role in limiting northward penetration of the post-separation meander in the nonlinear NOGAPS-forced simulations.

Only the NCEP-forced simulation continues to show EKWC overshoot at $1/32°$ resolution. It does form an eddy (in the mean) over the seamount at $38.3°$N, $129.8°$E, but there is sufficient negative wind-stress curl support that part of the EKWC continues northward all the way to Vladivostok as in the $1/8°$ linear and nonlinear simulations (Figs. 4h and 5h), including an offshore northward segment around $38°$N.

## 7. Deterministic vs. nondeterministic response to wind forcing

A series of six interannual simulations are used to quantify the relative influence of the deterministic response to the wind and throughflow forcing vs. the nondeterministic responses due to flow instabilities on the JES circulation. For this purpose, the six simulations used $1/32°$ resolution and were forced with the six-hourly ECMWF 10 m reanalysis winds over the time frame 1979–93. The 1979–93 ECMWF reanalysis also was used to create the climatological ECMWF 10 m and ECMWF 1000 mb reanalysis data sets described in Section 3. The initial state for the otherwise identical simulations was varied by starting each realization 1 month later from the climatologically forced $1/32°$ EC10M simulation after it reached statistical equilibrium. The atmospheric forcing also progressively started 1 month later in 1979.

Fig. 10 shows the annual mean SSH formed over 1991 from each of the six realizations. Because the six simulations were identical except for the initial state, the differences between them are due to mesoscale flow instabilities, and, as Fig. 10 demonstrates, the flow instabilities have a dramatic impact on the 1-year mean SSH and current pathways and their dynamics. We will briefly consider the post-EKWC separation pathway as an example. All realizations depict the EKWC separating near $37°$N, although there is substantial seasonal variation (seasonal means not shown). Case 1 has a post-EKWC separation pathway similar to the mean SSH from the $1/32°$ HR and EC1000 simulations (Fig. 8), while the others have post-separation current pathways more like the climatologically forced $1/32°$ EC10M simulation, but with varying indentation amplitudes on the east side of the meander and varying strengths of the nonlinear recirculation gyre. The significance and dynamics of the indentations are discussed in Section 6. There is no clear relation between the indentation amplitude and the northward penetration of the mean meander, although case 3 (which has the largest indentation) has the second lowest penetration latitude. Case 4 has the least northward penetration, the strongest nonlinear recirculation gyre,
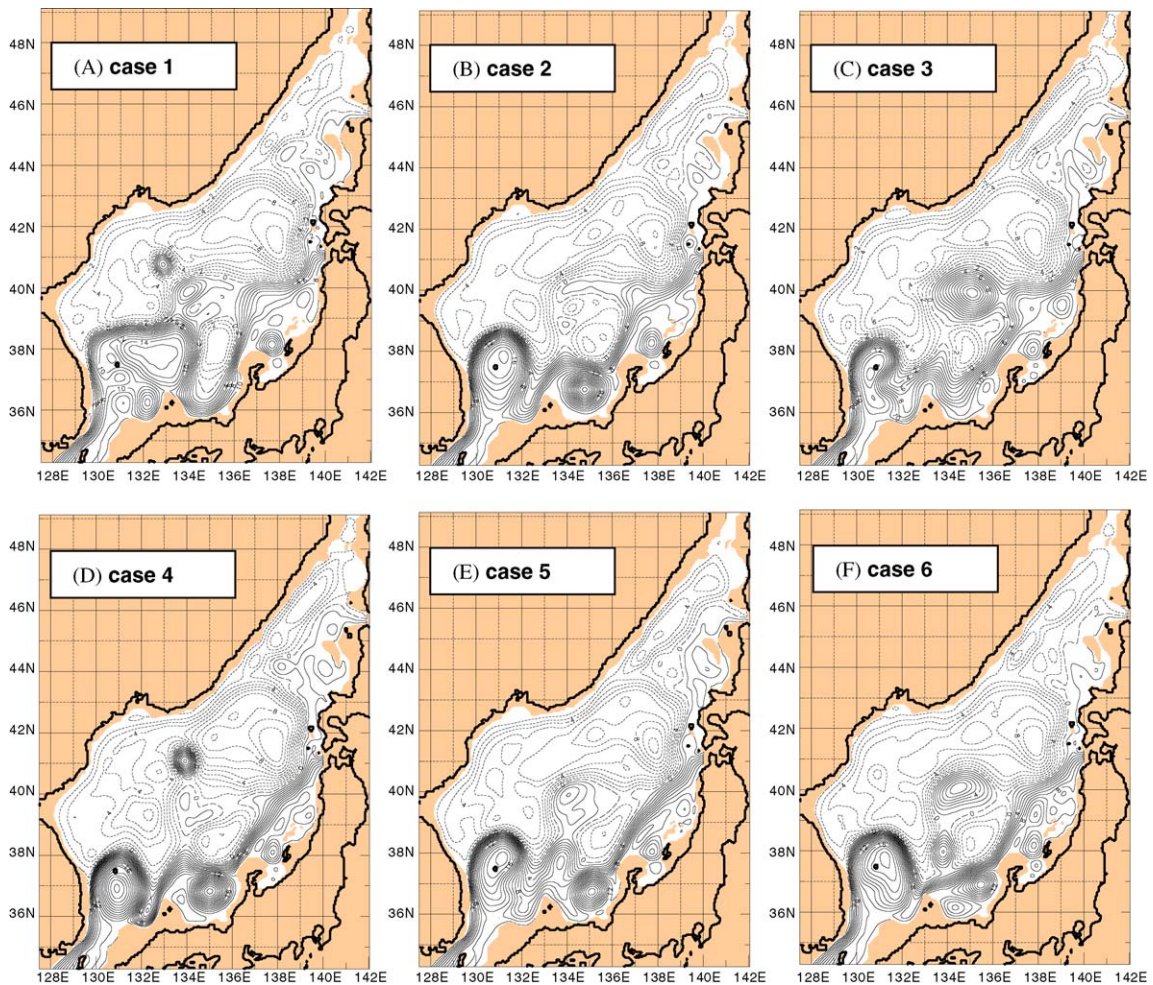
Fig. 10. Mean SSH for 1991 from six realizations of four-layer 1/32° NLOM forced with synoptic ECMWF 10 m reanalysis wind-stress. Each realization differs only by the initial state. Contour interval is 1 cm.

and the strongest EKWC and post-separation current. This could be due to abyssal current steering that produced the indentation in case 3 acting on a more inertial surface current or due to wavelength shortening (compared to a CAV trajectory) from baroclinic instability. All but cases 3 and 4 have a northward penetration latitude that would be limited by the eastward abyssal current along 38.5–38.8°N, a topic discussed in Section 6.

There are also significant variations in the flow patterns in the interior of the basin. Some cases (1 and 4; Figs. 10a and 10d) depict a relatively strong

anticyclonic eddy north of the subpolar front, a feature that to date is not supported by observations (to the authors' best knowledge). There is substantial variability in the position and size of the persistent (1-year mean) eddies, particularly in the southern part of the basin. The differences in the solutions shown in Fig. 10 are indicative of mesoscale flow instabilities, but to quantify the role of flow instabilities required further analysis as described below.

Metzger and Hurlburt (2001) describe a technique to separate the total variability field of model variables into two components, one which is a

deterministic response to the forcing and the other due to mesoscale flow instabilities (nondeterministic). The method, which reveals the relative importance of the two anomaly-generation mechanisms, is summarized as follows. First, the long-term mean (1979–93) SSH at each gridpoint is averaged over all realizations. This mean is then subtracted from the time series of each realization to form individual time series of anomaly fields ($\eta$). At each mesh point the temporally corresponding records of all realizations are averaged ($\bar{\eta}$) and deviations ($\eta' = \eta - \bar{\eta}$) are computed about the mean comprised of all realizations. These are then combined and averaged as follows:

$$\overline{\eta^2} = \overline{\bar{\eta}^2} + \overline{\eta'^2}, \tag{4}$$

where the bar represents the average overall realizations. Averaging over the same time period as the mean formed from all realizations, as was done here, ensures that the temporal average of the deterministic anomalies is zero. Now the right-hand side of (4) represents the deterministic variability due to atmospheric and throughflow forcing plus the variability due to flow instabilities, and the left-hand side is the total variability. Subsequently, each component can be divided by the total variability to determine the fractional amount of variability due to each, allowing assessment of the relative impact of flow instabilities and wind/throughflow forcing on model variability.

As explained and demonstrated by Metzger and Hurlburt (2001), a limited number of realizations can underestimate the nondeterministic fraction of variability due to flow instabilities and overestimate the deterministic component. Here, we constructed maps of the percent of deterministic vs. nondeterministic variability using the statistical technique described above for 2–6 realizations. The qualitative difference between these maps became progressively less as more solutions were included, and the difference between including five vs. six simulations (not shown) was quite small.

Fig. 11 shows the fractional variability for SSH, surface-layer velocities, and abyssal-layer eddy kinetic energy and pressure. The high values (dark red) indicate regions where flow instabilities are the primary source of variability and the dark blues where wind/throughflow forcing is the dominant source of variability. In Fig. 11a flow instabilities are the dominant source of SSH variability over much of the subpolar gyre between 37–38°N, where the EKWC separates from the coast of Korea, and following the general pathway of the subpolar front along the north rim of the Yamato Rise. The nondeterministic SSH variability along this pathway is a manifestation of inertial jets, meandering, and eddy activity associated with the subpolar front. The result that the SSH variability in the region where the EKWC separates from the coast of Korea is primarily due to flow instabilities indicates that the simulated variation in the location of separation (seasonal or otherwise) is associated mainly with instabilities of the jet rather than seasonal strengthening (weakening) of the subpolar gyre during the winter (summer) in response to wind forcing or the seasonal variation in the straits throughflow. However, north of the observed separation latitude ($> 38°N$) the SSH variability is deterministic, suggesting that the southward extent of the subpolar gyre, especially near East Korea Bay, is driven by the wind forcing and that the simulations contain little or no eddy shedding from the EKWC after it separates from the coast. In Section 6, we found that northward penetration of the post-separation current pathway tends to be limited by an eastward abyssal current along 38.5–38.8°N, consistent with the results in Fig. 11a–c.

Other regions where the SSH variability is deterministic include the deep areas over the Japan and Yamato Basins. This suggests that the bottom topography and abyssal flow strongly constrain the surface current pathways around these basins (Figs. 8 and 9). The ring of deterministic SSH variability around the edge of the entire basin is due to wind-forced coastally trapped internal Kelvin waves and the quasigeostrophic constraint that requires constant stream function along closed boundary segments (Kelvin waves are not quasigeostrophic). The determinicity of surface-layer velocity components variability (Figs. 11b and c) is generally similar to the SSH variability patterns, except in the region of the Ulleung Basin.
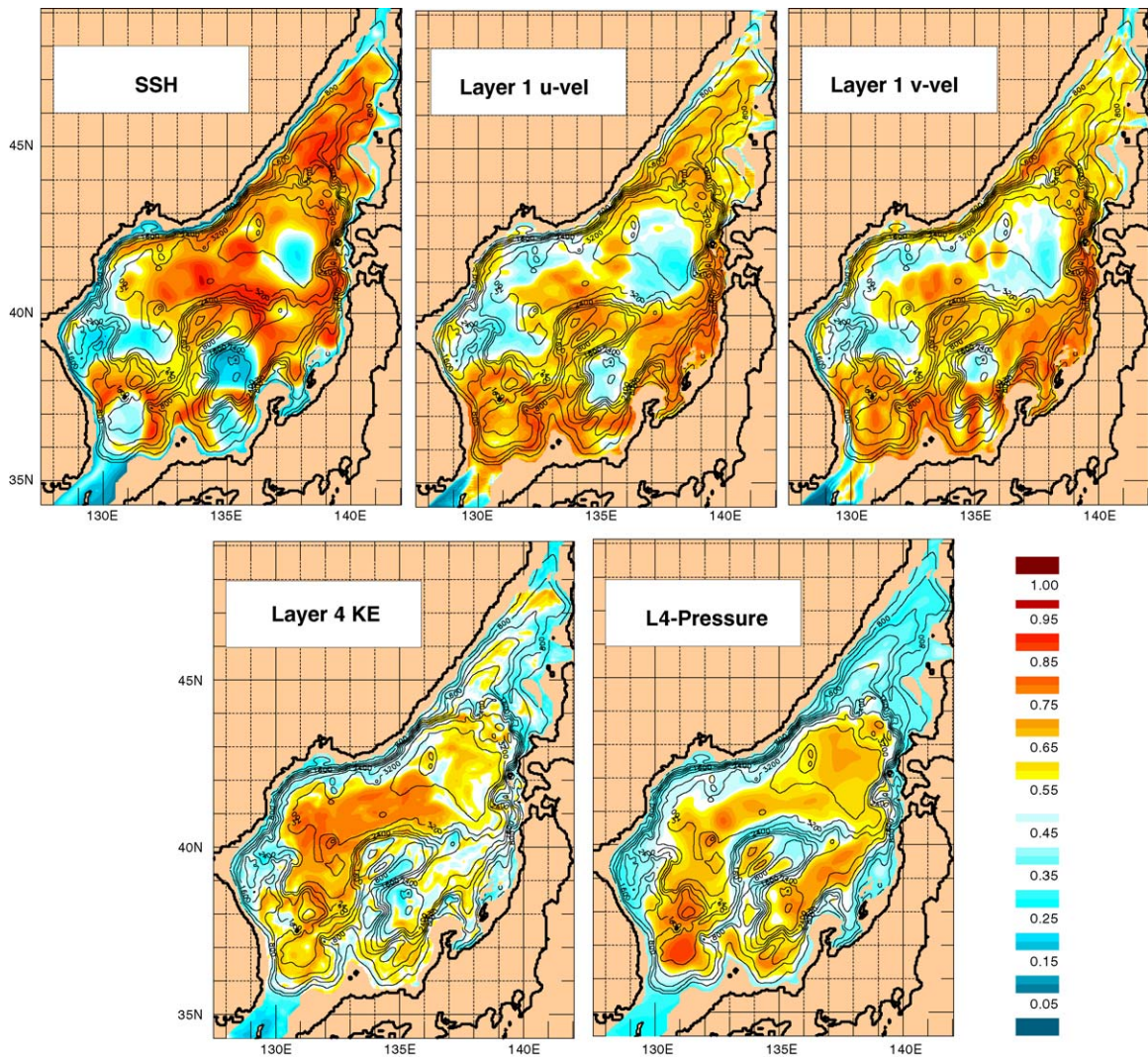
Fig. 11. The fraction of the modeled variability from four-layer $1/32°$ NLOM for (A) SSH, (B) $u$-component of surface layer velocity, (C) $v$-component of surface-layer velocity, (D) abyssal-layer eddy kinetic energy, and (E) abyssal-layer pressure deviation. The blue areas are predominantly deterministic (caused by direct wind forcing) and the red/orange areas are predominantly nondeterministic (caused by flow instabilities).

Immediately surrounding most of the Ulleung Basin, the SSH variability is highly nondeterministic. Taken with the pattern of nondeterminicity in the abyssal layer, this pattern is consistent with baroclinic instability surrounding the Ulleung Basin in the surface layer. The instability transfers energy to the abyssal layer, where the flow is inhibited from crossing the geostrophic ($f/h$) contours of the topography to satisfy conservation

of potential vorticity. Thus, the EKE is largely transferred to the interior of the Ulleung Basin, and the resulting KEM (Fig. 9) predominates in following the $f/h$ contours of the bottom topography. The relatively uniform pattern of abyssal pressure nondeterminicity covering the abyssal plain of the Ulleung Basin and nondeterminicity of P4 > KE4 indicates that the nondeterministic P4 variations are typically the scale of the Ulleung

Basin abyssal plain. Overall, the nondeterministic fraction of the abyssal variability is predominantly confined to areas where the bottom topography is relatively flat, such as the Japan Basin abyssal plain, the Yamato Trough, and Ulleung Basin.

## 8. Summary and conclusions

Seven different monthly wind-stress climatologies (Hellerman and Rosenstein, COADS, Na, ECMWF 10 m, ECMWF 1000 mb, NOGAPS and NCEP) were used to force a suite of linear and nonlinear simulations in order to elucidate the sensitivity of JES simulations to the choice of wind-forcing product, including the impact on the model dynamics. Seasonally varying straits throughflow forcing was included in all the simulations, and the impact of throughflow forcing in the absence of winds was also investigated. The linear solutions provide deterministic information of the impact of the wind forcing without the complications of higher-order dynamics. Those higher-order dynamics, however, provide the ingredients needed for the realistic representation of many of the circulation features. Nonlinear simulations with both 1/8° resolution (weak flow instabilities) and 1/32° (strong flow instabilities) were used.

The linear simulations include only the lowest-order dynamics, mainly a Munk $\beta^{1/3}$ viscous boundary layer with a Sverdrup (1947) interior. In the absence of wind forcing, the TWC hugs the western boundary as a Munk $\beta^{1/3}$ viscous boundary layer until it is forced to separate from the coast of Korea and flow eastward to satisfy the constraints of the Tsugaru and Soya outflow ports. Thus, contrary to what is observed, there is northeastward flow along the coast of Siberia and extremely weak flow along the coast of Honshu. When winds are added, in all cases net positive wind-stress curl in the northern part of the domain results in overall cyclonic flow in the subpolar gyre, including southwestward flow along the coast of Siberia. In most cases the separation latitude of the EKWC is still determined by the latitude of Tsugaru Strait (too far north), although some of this flow continues

northward on the eastern side of the basin and exits through Soya. The same simulations also depict southwestward flow along part or all of the Honshu coast, contrary to observations. The NCEP-forced simulation stands alone in depicting northeastward flow along the entire Honshu coast as observed, but is the only linear simulation that lacks an EKWC and overall is the least realistic (a clear outlier).

The nonlinear simulations include the addition of bottom topography, multiple internal modes, diapycnal mixing, and ventilation of layer interfaces. At 1/8° resolution, these additions allow the possibility of isopycnal outcropping, the formation of inertial boundary layers and jets, and weak barotropic/baroclinic flow instabilities. At this resolution, mean abyssal currents are weak and driven predominantly by deep vertical mixing in the subpolar gyre. At 1/32° the transfer of energy from the upper ocean to the abyssal layer via baroclinic instability is much stronger, driving stronger mean abyssal currents that have a more significant influence on mean surface current pathways than at 1/8°, i.e. much stronger upper ocean–topographical coupling.

In general, most of the simulations reproduce the large-scale circulation features of the JES when compared to schematic charts of the circulation. In particular, all depict cyclonic circulation in the subpolar gyre due to positive wind-stress curl, which results in regional upwelling due to Ekman suction, isopycnal outcropping, and diapycnal mixing. Likely areas of intermediate- and/or deep-water formation occur where the deepest interface ventilates (or the isopycnals outcrop), particularly over a long time period. However, substantial variability in the strength, size, and location of the subpolar gyre and the deep interface ventilation exists. In addition, all of the nonlinear simulations (including the simulation with straits throughflow forcing only) simulate the northeastward NB of the TWC along the Honshu coast. This is due to isopycnal outcropping in the simulations, as explained by Hogan and Hurlburt (2000).

Simulation of the EKWC separation latitude (37–38°N) from the coast of Korea has proven to be one of the more challenging problems in JES modeling. Hogan and Hurlburt (2000) identified

two distinct mechanisms that could yield a realistic separation latitude for the EKWC, wind-stress curl and upper ocean–topographical coupling, the latter only occurring in the $1/32°$ simulations. However, the wind-stress curl mechanism is ineffective in the linear simulations and only one gives a separation latitude south of Tsugaru Strait ($\sim$41°N). That is the NOGAPS-forced simulation, which gives separation at $\sim$39°N. In this study, we found that when part of the flow through Tsushima Strait is diverted into the NB (as in all the nonlinear simulations), the wind-stress curl mechanism is better able to compete with the straits throughflow and gives a realistic EKWC separation latitude in the $1/8°$ nonlinear simulations forced by Na, ECMWF 10 m, and NOGAPS and marginally realistic separation with ECMWF 1000 mb and NCEP forcing. The simulations forced with Hellerman-Rosenstein, COADS, and throughflow only still show EKWC overshoot with separation at $\sim$40°N. At $1/32°$ resolution five of the six simulations show realistic EKWC separation, the Na, ECMWF 10 m, and NO-GAPS-forced via the wind-stress mechanism as before, the Hellerman–Rosenstein and ECMWF 1000 mb via the upper ocean–topographical coupling mechanism. Hogan and Hurlburt (2000) discuss EKWC separation via the upper ocean–topographical coupling mechanism for the Hellerman–Rosenstein-forced simulation in detail. $1/32°$ throughflow only and COADS-forced simulations were omitted because of similarity to the Hellerman–Rosenstein-forced simulation at $1/8°$ resolution. These would probably also give a realistic EKWC separation latitude at $1/32°$ resolution via the upper ocean–topographical coupling mechanism. At $1/32°$ resolution only the NCEP-forced simulation shows EKWC overshoot (to $\sim$43°N). This is due to strong wind-stress curl support for a northward western boundary current between 39°N and 43°N as seen in the linear simulation.

At $1/32°$ all of the simulations except the NCEP-forced show a strong influence of the Yamato Rise on the path of the subpolar front due to steering by abyssal currents. The $1/32°$ NCEP-forced simulation does not show this because the subpolar front approaches the Yamato Rise from the northwest in that case. The path of the

subpolar front in the $1/8°$ NOGAPS and ECMWF 10 m-forced simulations is also influenced by the Yamato Rise. Of the $1/8°$ simulations, the NOGAPS-forced simulation has the strongest abyssal currents. These are driven by the strongest isopycnal outcropping and vertical mixing in the subpolar gyre. In this case, some of the vorticity produced by the wind-stress curl is transferred directly into the abyssal layer. This is the reason it is quite similar to the corresponding $1/32°$ simulation despite differences in the abyssal forcing mechanisms (isopycnal outcropping at $1/8°$ and strong baroclinic instability at $1/32°$). In the $1/8°$ ECMWF 10m-forced simulation, weaker abyssal currents around the Yamato Rise are aided by an overlying region of strong negative wind-stress curl not seen in the other wind sets.

Synoptic wind forcing was used to investigate determinicity vs. nondeterminicity of interannual variability in $1/32°$ simulations forced with the 1979–93 six-hourly ECMWF 10-m reanalysis wind-stresses and seasonally varying flows through the straits. Mean SSH from six simulations that differed only in the initial state show significantly different mean current pathways in 1-year means over the same year. The differences are primarily due to flow instabilities, which are well resolved at $1/32°$ resolution. The fraction of variability due to flow instabilities (the nondeterministic component) and wind/throughflow forcing (the deterministic component) was calculated, and indicates that flow instabilities are responsible for most of the SSH variability in the region where the EKWC separates from the coast of Korea ($\sim$37–38°N), extending along the pathway of the subpolar front to the Tsugaru Strait. These instabilities are associated with the inertial character of the EKWC recirculation gyre (the Ulleung eddy) and meandering and frontal eddy activity associated with the subpolar front. SSH variability is largely deterministic in the coastal Kelvin waveguide and over some deep basins and troughs. Abyssal variability of pressure and eddy kinetic energy was nondeterministic over areas with relatively flat topography, indicative of the constraint that deep flows tend to follow geostrophic ($f/h$) contours when $|\nabla(f/h)|$ is large.

Collectively, the simulations forced with the different wind sets show a much wider range of

features and dynamics than obtained using a single wind set. Thus, they give a broader perspective on the JES circulation and the range of features and dynamics it may exhibit than found in the simulations driven by any single atmospheric forcing product. Based on the mean circulation, overall the most realistic simulations (all nonlinear) are the 1/32° ECMWF 1000 mb forced, the 1/8° and 1/32° Na forced, and the 1/32° NOGAPS forced. The least realistic nonlinear simulations are the 1/8° and 1/32° NCEP forced. This is based on general agreement with the schematics and other known features of the circulation. Although wind forcing strongly affects the circulation features and current pathways in the JES, other mechanisms, both physical and dynamical, also play an important role. The upper ocean–topographical coupling described in Hogan and Hurlburt (2000) is an example of a dynamical mechanism. Other physical mechanisms such as buoyancy forcing, accurate mixed-layer representation, and realistic straits throughflow, and the nonlinear combination of all, undoubtedly play an important role as well.

## Acknowledgments

## References

Bunker, A.F., 1976. Computations of surface energy flux and annual air–sea interaction cycles of the North Atlantic Ocean. Monthly Weather Review 104, 1122–1140.

Cardone, V.J., 1969. Specification of the wind distribution in the marine boundary layer for wave forecasting. New York School of Engineering and Science, Report GSL-TR69-1, 181pp.

da Silva, A.M., Young, C.C., Levitus, S., 1994a. Algorithms and procedures. Atlas of Surface Marine Data 1994, vol. 1, NOAA Atlas NESDIS 6, US Department of of Commerce, NOAA, NESDIS, 83pp.

da Silva, A.M., Young, C.C., Levitus, S., 1994b. Anomalies of heat and momentum fluxes. Atlas of Surface Marine Data 1994, vol. 8, NOAA Atlas NESDIS 8, US Department of of Commerce, NOAA, NESDIS, 413pp.

Garratt, J.R., 1977. Review of drag coefficients over oceans and continents. Monthly Weather Review 105, 915–929.

Gibson, J.K., Kallberg, P., Uppala, S., Hernandez, A., Nomura, A., Serrano, E., 1997. ECMWF Re-Analysis Project Report Series: 1. ERA Description. ECMWF, Reading, Berkshire, UK, 71pp.

Hellerman, S., Rosenstein, M., 1983. Normal monthly wind-stress over the world ocean with error estimates. Journal of Physical Oceanography 13, 1093–1104.

Hogan, P.J., Hurlburt, H.E., 2000. Impact of upper ocean–topographical coupling and isopycnal outcropping in Japan/East Sea simulations with 1/8° to 1/64° resolution. Journal of Physical Oceanography 30, 2535–2561.

Hogan, T.F., Rosmond, T.E., 1991. The description of the Navy Operational Global Atmospheric Prediction System's spectral forecast model. Monthly Weather Review 119, 1786–1815.

Holloway, G., Sou, T., Eby, M., 1995. Dynamics of the circulation of the Japan Sea. Journal of Marine Research 53, 539–569.

Hurlburt, H.E., Thompson, J.D., 1980. A numerical study of Loop Current intrusions and eddy shedding. Journal of Physical Oceanography 10, 1611–1651.

Hurlburt, H.E., Thompson, J.D., 1982. The dynamics of the Loop Current and shed eddies in a numerical model of the Gulf of Mexico. In: Nihoul, J.C.J. (Ed.), Hydrodynamics of semi-enclosed seas. Elsevier, Amsterdam, pp. 243–297.

Kalnay, E., Kanamitsu, M., Kistler, R., Collins, W., Deaven, D., Gandin, L., Iredell, M., Saha, S., White, G., Woolen, J., Zhu, Y., Chelliah, M., Ebisuzaki, W., Higgins, W., Janowiak, J., Mo, K.C., Ropelewski, C., Wang, J., Leetma, A., Reynolds, R., Jenne, R., Joseph, D., 1996. The NCEP/NCAR 40-Year Reanalysis Project. Bulletin of the American Meteorological Society 77, 437–471.

Kawabe, M., 1982. Branching of the Tsushima Current in the Japan Sea. II. Numerical experimentation. Journal of the Oceanographical Society of Japan 38, 183–192.

Kim, C.-H., Yoon, J.H., 1996. Modeling of the wind-driven circulation in the Japan/East Sea using a reduced-gravity model. Journal of Oceanography 52, 359–373.

Kim, C.-H., Yoon, J.-H., 1999. A numerical modeling of the upper and the intermediate layer circulation in the East Sea. Journal of Oceanography 55, 327–345.

Metzger, E.J., Hurlburt, H.E., 2001. The nondeterministic nature of the Kuroshio pepentration and eddy shedding in

the South China Sea. Journal of Physical Oceanography 31, 1712–1732.

Moore, D.R., Wallcraft, A.J., 1998. Formulation of the NRL Layered Ocean Model in spherical coordinates, NRL Technical Report NRL/CR/7323—96-0005, 24 pp.

Morimoto, A., Yanagi, T., 2001. Variability of sea surface circulation in the Japan Sea. Journal of Oceanography 57, 1–13.

Munk, W.H., 1950. On the wind-driven ocean circulation. Journal of Meteorology 7, 79–93.

Na, J.-Y., Seo, J.-W., Han, S.-K., 1992. Monthly mean sea surface winds over the adjacent seas of the Korea Peninsula. Journal of the Oceanological Society of Korea 27, 1–10.

Na, J.-Y., Seo, J.-W., Lie, H.-J., 1999. Annual and seasonal variations of the sea surface heat fluxes in the East Asian marginal seas. Journal of Oceanography 55, 257–270.

Naganuma, K., 1977. The oceanographic fluctuations in the Japan Sea. Kaiyo Kayaku 9, 137–141.

Orlanski, I., 1976. A simple boundary condition for unbounded hyperbolic flows. Journal of Computational Physics 21, 251–269.

Preller, R.H., Hogan, P.J., 1998. Oceanography of the Sea of Okhotsk and the Japan/East Sea. In: Robinson, A.R., Brink, K.H. (Eds.), The Sea, vol. 11: The Global Coastal Ocean, Regional Studies and Synthesis. Wiley, New York, pp. 429–481.

Sekine, Y., 1991. A numerical experiment on the seasonal variation of the oceanic circulation in the Japan Sea. In: Takano, K. (Ed.), Oceanography of Asian Marginal Seas, Elsevier Oceanography Series, vol. 54. Elsevier, Amsterdam, pp. 113–128.

Senjyu, T., 1999. The Japan Sea Intermediate Water; its characteristics and circulation. Journal of Oceanography 55, 111–122.

Senjyu, T., Sudo, H., 1994. The upper portion of the Japan Sea Proper Water: Its source and circulation as deduced from isopycnal analysis. Journal of Oceanography 50, 663–690.

Senjyu, T., Shin, H.-Y., Yoon, J.-H., Nagano, Z., An, H.-S., Byun, S.-K., Lee, C.-K., 2002. Deep flow field in the Japan/East Sea as deduced from direct current measurements. Deep-Sea Research II, this issue [doi:10.1016/j.dsr2.2003.10.013].

Seung, Y.-H., 1992. A simple model for separation of the East Korean Warm Current and formation of the North Korean Cold Current. Journal of the Oceanological Society of Korea 27, 189–196.

Seung, Y.-H., Kim, K.-J., 1993. A numerical modeling of the East Sea circulation. Journal of the Oceanological Society of Korea 28, 292–304.

Seung, Y.-H., Yoon, J.-H., 1995. Some features of wintertime convection in the Japan Sea. Journal of Oceanography 51, 61–73.

Shin, C.-W., Kim, C., Byun, S.-K., 2001. The warm eddy in the East Korean Bight. Ocean and Polar Research 23, 1–10.

Suh, Y.-S., Mitchell, B.G., Lim, K.-S., 1999. A recurring eddy off the Korean northeast coast captured on satellite ocean color and sea surface temperature imagery. Journal of the Korean Society of Remote Sensing 15, 175–181.

Sverdrup, H.U., 1947. Wind-driven currents in a baroclinic ocean: With application to the equatorial currents of the eastern Pacific. Proceedings of the National Academy of Science USA 33, 318–326.

Takematsu, M., Nagano, Z., Ostrovskii, A.G., Kim, K., Volkov, Y., 1999. Direct measurements of deep currents in the northern Sea of Japan. Journal of Oceanography 55, 207–216.

Townsend, T.L., Hurlburt, H.E., Hogan, P.J., 2000. Modeled Sverdrup flow in the North Atlantic from 11 different wind-stress climatologies. Dynamics of Atmospheres and Oceans 32, 373–417.

Wallcraft, A.J., 1991. The Navy Layered Ocean Model Users Guide. NOARL Report 35, Naval Research Laboratory, Stennis Space Center, MS, 21pp. (available from Naval Research Laboratory, Stennis Space Center, MS 39529).

Wallcraft, A.J., Moore, D.R., 1997. A scalable implementation of the NRL Layered Ocean Model. Parallel Computing 23, 227–2242.

Woodruf, S.D., Slutz, R.J., Jenne, R.L., Steurer, P.M., 1987. A comprehensive ocean–atmosphere data set. Bulletin of the American Meteorological Society 68, 1239–1250.

Yarachin, V.G., 1980. Steady state of the Japan Sea circulation. In: Pokudov (Ed.), Problems in Oceanography, Hydro-meteoidat, pp. 46–61 (in Russian).

Yoon, J.-H., 1982. Numerical experiment on the circulation in the Japan Sea. Part III, mechanism of the Nearshore Branch of the Tsushima Current. Journal of the Oceanographical Society of Japan 38, 125–130.